DOKUZ EYLÜL UNIVERSITY
GRADUATE SCHOOL OF NATURAL AND APPLIED SCIENCES

GEMMOLOGICAL AND MINERALOGICAL INVESTIGATIONS AND GENESIS OF THE MASSIVE DARK GREEN CHRYSOPRASE FROM THE BİGA-ÇANAKKALE REGION

by
Ufuk ÖREN

February, 2012
İZMİR

GEMMOLOGICAL AND MINERALOGICAL INVESTIGATIONS AND GENESIS OF THE MASSIVE DARK GREEN CHRYSOPRASE FROM THE BİGA-ÇANAKKALE REGION

A Thesis Submitted to the
Graduate School of Natural and Applied Sciences of Dokuz Eylül University
In Partial Fulfillment of the Requirements for the Degree of Master of Science
in Natural Building Stones and Gem Stones Programme

by
Ufuk ÖREN

February, 2012
İZMİR

M.Sc. THESIS EXAMINATION RESULT FORM

We have read the thesis entitled **"GEMMOLOGICAL AND MINERALOGICAL INVESTIGATIONS AND GENESIS OF THE MASSIVE DARK GREEN CHRYSOPRAS FROM THE BİGA-ÇANAKKALE REGION"** completed by **UFUK ÖREN** under supervision of **ASSOC. PROF. DR. MURAT HATİPOĞLU** and we certify that in our opinion it is fully adequate, in scope and in quality, as a thesis for the degree of Master of Science.

Assoc. Prof. Dr. Murat HATİPOĞLU

Supervisor

Prof. Dr. Turgay Onargan

(Jury Member)

Doç. Dr. Talip Güngör

(Jury Member)

Prof. Dr. Mustafa SABUNCU
Director
Graduate School of Natural and Applied Sciences

ACKNOWLEDGMENTS

First of all, I would like to express my gratitude and my special thanks to my supervisor Assoc. Prof. Dr. Murat Hatipoğlu, Dokuz Eylül University, for his guidance, patience and support, as well as his understanding. I appreciate his time and effort in helping me to write this thesis and greatly value his assistance.

In addition, during the obtaining of the analytical data, I am grateful to Gökhan Gümüş, who is the director of the Laboratory of Batı Anadolu Cement Factory, for the X-ray diffraction graphics, to Asst. Yasemin Tuncer-Arslanlar and Prof. Dr. Nurdoğan Can, from Celal Bayar University, for sharing the luminescence spectra, and also to Asst. Prof.Dr. İbrahim Gündoğan and Salim Özcan, from the department of Geological Engineering of Dokuz Eylül University, for preparing and evaluating the petrographic thin sections.

And of course, I would like to give my endless affection to Lec. Hakkı Babalık, Halil Sarp, my family and my parents, for their support and encouragement in everything I do. Thank you!

Ufuk ÖREN

GEMMOLOGICAL AND MINERALOGICAL INVESTIGATIONS AND GENESIS OF THE MASSIVE DARK GREEN CHRYSOPRAS FROM THE BİGA-ÇANAKKALE REGION

ABSTRACT

While the major commercial chrysoprase deposits in Turkey are present in about five different regions, namely Çanakkale, Eskişehir, Bilecik, Erzurum and Mardin, the most important deposit of gem-quality chrysoprase is located in the Biga–Çanakkale region. Therefore, the present study is focused on the Biga chrysoprase deposit, which is found as fracture fillings covered with a weathering crust in the silicified serpentinites throughout the border of a metamorphic zone. Several previously undocumented characteristics of Biga chrysoprase are described for the first time during this investigation. Some of the Biga chrysoprase samples have been cut and polished into cabochons and slabs as gem objects to show its typical color and quality.

Average bulk (XRF) and trace element (ICP-AES) chemical analyses reveal relatively higher concentrations of some trace elements, such as Fe, Cr, Mn, As, Ni, Pb, Sb, and Zn are characteristics for Biga chrysoprase. Some of these elements can be found in any chrysoprase sample from Poland, Kazakhistan, Australia or Tanzania, even though the concentrations of some are unusual.

In addition to other well-known analytical methods, Dispersive confocal micro-Raman spectroscopy (DCμRS), was used to characterize and identify in detail the Biga Chrysoprase samples. Accordingly, the strong micro-Raman bands that peaked at 1577, 1430, 1303, 1160, 1082, 549, 501, 460, 394, 352, 259, 206, 139 and 126 cm-1 are characteristics of Biga Chrysoprase.

Biga chrysoprase samples also show numerous broad and intensive luminescence bands. Three different luminescence spectra of the Biga chrysoprase

[photoluminescence (PL), cathodoluminescence (CL), and thermoluminescence (TL)] were taken into consideration, and evaluated.

Finally, gemmological, mineralogical and spectroscopical data provide positive identification of the provenance of Biga chrysoprase. It can be seen that the these data provide a unique fingerprint for this kind of chrysoprase gem material.

Keywords: Chrysoprase, gemmology, dispersive (green laser) confocal micro-Raman spectroscopy, x-ray fluorescence, trace elements, luminescence, Çanakkale-Biga.

BİGA-ÇANAKKALE BÖLGESİNİN KÜTLESEL YAPILI KOYU YEŞİL KRİZOPRASIN GEMOLOJİK VE MİNERALOJİK İNCELEMESİ VE OLUŞUM KÖKENİNİN BELİRLENMESİ

ÖZ

Her nekadar Türkiye'deki başlıca ticari krizopras yatakları, yaklaşık beş bölge içerisinde yani Çanakkale, Eskişehir, Bilecik, Erzurum ve Mardin, bulunsa bile, süstaşı kalitesindeki krizoprasın en önemli yatağı, Biga-Çanakkale bölgesinde yer almaktadır. Bu nedenle, mevcut çalışma, bir metamorfik kuşağın sınırı boyunca silisleşmiş serpantinitlerlerdeki ayrışmış bir kabukla örtülmüş çatlak dolgusu olarak bulunan Biga krizopras yatağı üzerine odaklanmıştır. Bunun bir sonucu olarak, Biga krizoprasının önceden yazılmamış çok sayıdaki karekteristikleri bu çalışma süresince ilk kez tanımlanmıştır. Biga krizopras örneklerinin bazıları, tipiksel renk ve kaliteyi göstermek için kabaşonlar ve dilimler halinde çok sayıda süstaşı objeleri olarak kesilmiş ve parlatılmıştır.

Ortalama hacimsel (XRF) ve iz element (ICP-AES) kimyasal analizler ortaya çıkarmıştır ki, bazı iz elementlerin, örğ. Fe, Cr, Mn, As, Ni, Pb, Sb ve Zn göreceli yüksek konsantrasyonları, Biga krizoprası için karakteristiktir. Bu iz elementlerin birkaçı, Polonya'dan, Kazakistan'dan ve Tanzanya'dan elde edilen herhangi bir krizopras örneği içerisinde mevcut olabilir, ancak bunlardan bazıların konsantrasyonları sıra dışıdır.

Biga krizopras örnekleri, saçınımsal konfokal mikro-Raman spectroskopisi (DCμRS) ve de diğer iyi bilinen analitiksel metotlar kullanarak karakterize etmek ve detaylı tanımlamak için incelenmişlerdir. Buna göre, 1577, 1430, 1303, 1160, 1082, 549, 501, 460, 394, 352, 259, 206, 139 ve 126 cm-1'lerde piklenmiş güçlü mikro-Raman bandları, Biga krizoprasının karakteristikleridir.

Diğer yandan, Biga krizopras örnekleri çok sayıda geniş ve şiddetli lüminesans bandları gösterirler. Biga krizoprasının üç farklı lüminesans spektraları

[fotolüminesans (PL), kathodolüminesans (CL) ve termolüminesans (TL)] göz önüne alınmış ve değerlendirilmiştir.

Sonuç olarak, gemolojiksel, mineralojiksel ve spektroskopsal deliller, Biga krizoprasının coğrafik oluşum kökeniyle ilgili kesin ve olumlu tanımlamalar sağlarlar. Görülmektedir ki, elde edilen bu veriler bu cins krizopras süstaşı için özgün anahtar işaretler vermektedir.

Anahtar Sözcükler: Krizopras, gemoloji, saçınımsal (yeşil lazer) konfokal mikro-Raman spektroskopisi, x ışını floresansı, eser element, lüminesans, Çanakkale-Biga.

CONTENTS

Page

THESIS EXAMINATION RESULT FORM.....ii
ACKNOWLEDGEMENTS.....iii
ABSTRACT.....iv
OZ.....vi

CHAPTER ONE – INTRODUCTION.....1

1.1 Nomenclature and History of Chrysoprase.....1
1.2 Chrysoprase in Turkey.....2
1.3 Advantages of a Non-Destructive (Raman) Further Spectroscopical Method in the Case of Gemstone Characterization.....5
1.4 Advantages of a Destructive (Luminescence) Further Spectroscopical Method in the Case of Gemstone Characterization.....6
1.5 Aims and Scope.....8

CHAPTER TWO – MATERIALS AND METHODS.....9

2.1 Materials.....9
2.2 Instrumental Methods.....9

CHAPTER THREE – RESULTS AND DISCUSSION.....17

3.1 Provenance and Genesis of Biga Chrysoprase.....17
3.2 Lapidary.....21
3.3 Polarizing Microscopy (PM).....25
3.4 X-Ray Diffractometry (XRD).....28
3.5 Infrared Spectroscopy (IRS).....32
3.6 Chemistry (XRF and ICP-AES).....33
3.7 Dispersive (Green Laser) Confocal Micro-Raman Spectroscopy (DCμRS)...35

3.8 Optical Absorption Spectroscopy (OAS).....46
3.9 Luminescence (PL, CL, TL).....48
3.9.1 Photoluminescence (PL).....49
3.9.2 Cathodoluminescence (CL).....51
3.9.3 Thermoluminescence (TL).....55

CHAPTER FOUR – CONCLUSIONS.....57

REFERENCES.....60

CHAPTER ONE
INTRODUCTION

1.1 Nomenclature and History of Chrysoprase

Chrysoprase is a dark and/or dull green-colored sub-variety of the microcrystalline quartz group, consisting mainly of optical length-fast chalcedony (Rossman, 1994; Back and Mandarino, 2008). The origin of the name is Greek for "gold leek" (Mitchell, 1979). The material is micro fibrous, and sometimes contains fine-grained silica (Frondel, 1978). Chrysoprase is in high demand in terms of gemmological importance (Schumann, 1984; Arem, 1987). Chrysoprase is prized for its often jade-green color, although its color varies from olive-green to a pale sea green. However, many chrysoprase roughs are often interlaced with a brownish crust of ferric hydroxide.

Chrysoprase has been identified in ancient Egyptian artifacts, some of which have been dated to the Predynastic Period (Lucas, 1989). However, the first significant deposit for chrysoprase in Europe was found in Lower Silesia, in Szklary near Zabkowice Slaskie in Poland, in 1425 (Sachanbinski et al., 2001). Therefore, chrysoprase was used as a decorative stone during the European Middle Ages. Accordingly, chrysoprase has been worked as many architectural objects (artifacts) since ancient times. For instance, chrysoprase was very popular in the 14th century when the Holy Roman Emperor Charles IV used it to decorate chapels, including the Chapel of Saint Wenceslas in Prague (Sachanbinski et al., 2001).

Today, the worldwide commercial deposits of chrysoprase are still rarely found. These deposits are mainly located in Australia (Nagase et al., 1997; Befi, 2009), in Poland (Sachanbinski et al., 2001; Skrzypek et al., 2003 and 2004), in Kazakhstan (Sachanbinski et al., 2001; Witkowski and Zabinski, 2004), in Brazil (Komov et al., 1994), in Tanzania (Witkowski and Zabinski, 2004; Shigley et al., 2009; Graetsch, 2011), and in Turkey as well.

1.2 Chrysoprase in Turkey

When the geological formation conditions are considered, it is highly probable that there are many chrysoprase-bearing localities in Turkey. However, it can be stated that there are about five locations of chrysoprase mine fields in terms of commercial quantities. These locations and their typical chrysoprase yields are shown in Figure 1.1. However, it is well-known that the most important chrysoprase pit is near the village of Dikmen in the Biga–Çanakkale region (Figure 1.2), and the pit has been mined since the Ottoman Period (from at least the 1700s to now) (Figure 1.3).

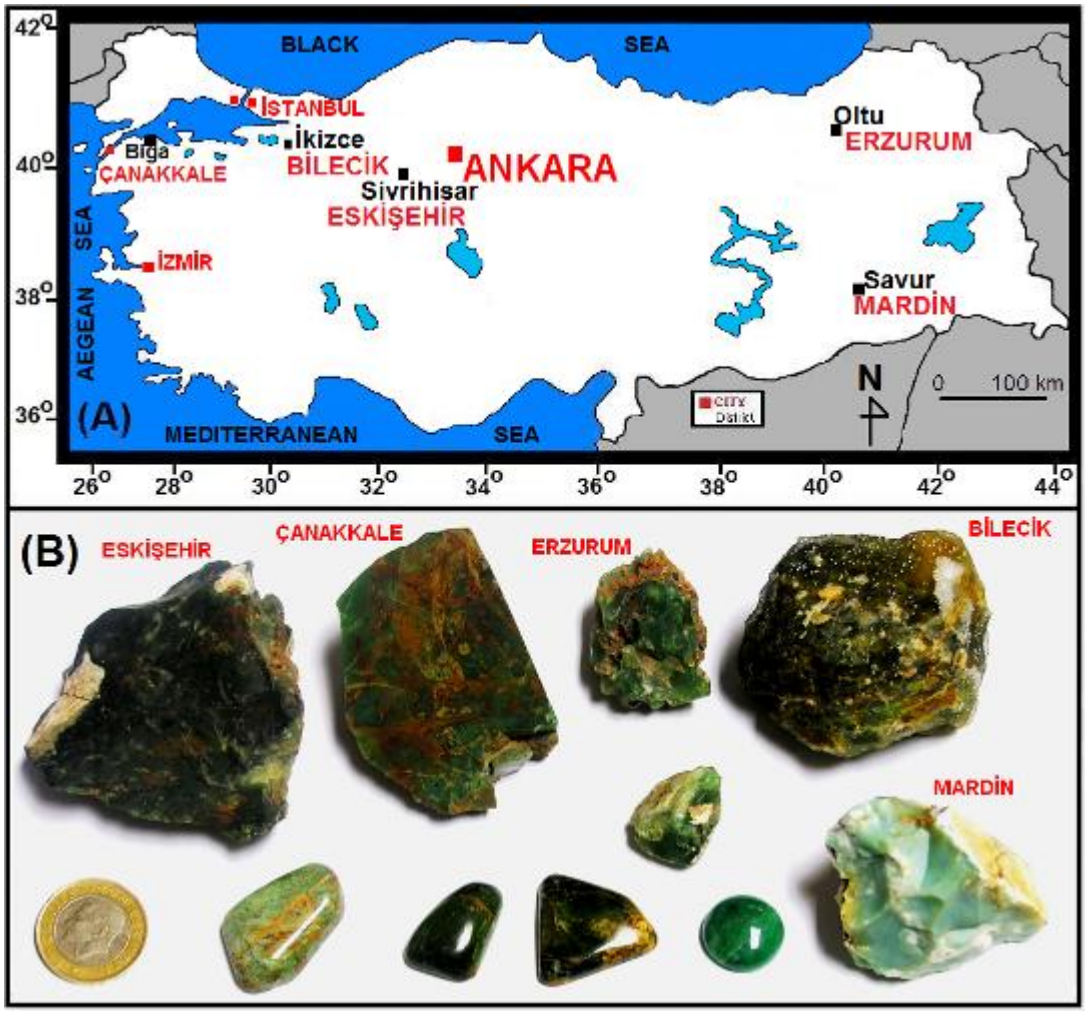

Figure 1.1 Chrysporase mine fields in Turkey **(A)**. Some chrysoprase rough and polished samples obtained from these localities **(B).**

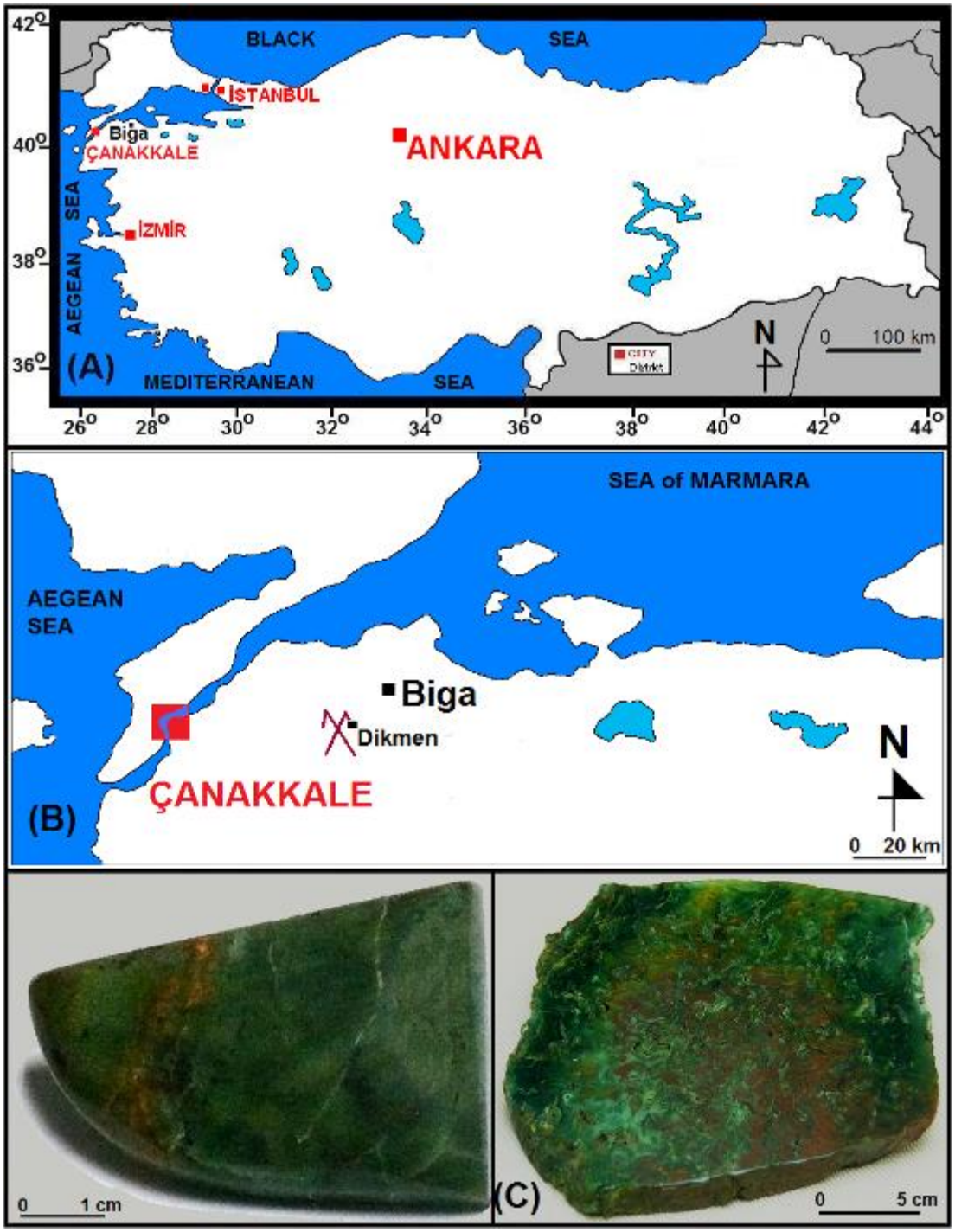

Figure 1.2 Location map showing the Biga-Çanakkale region in Turkey **(A)**, and enlarged map comprising the village of Dikmen in the Biga–Çanakkale region, where the commercial quantities of gem-quality massive chrysoprase masses are located **(B)**. Two representative Biga chrysoprase slabs cut and polished **(C)**.

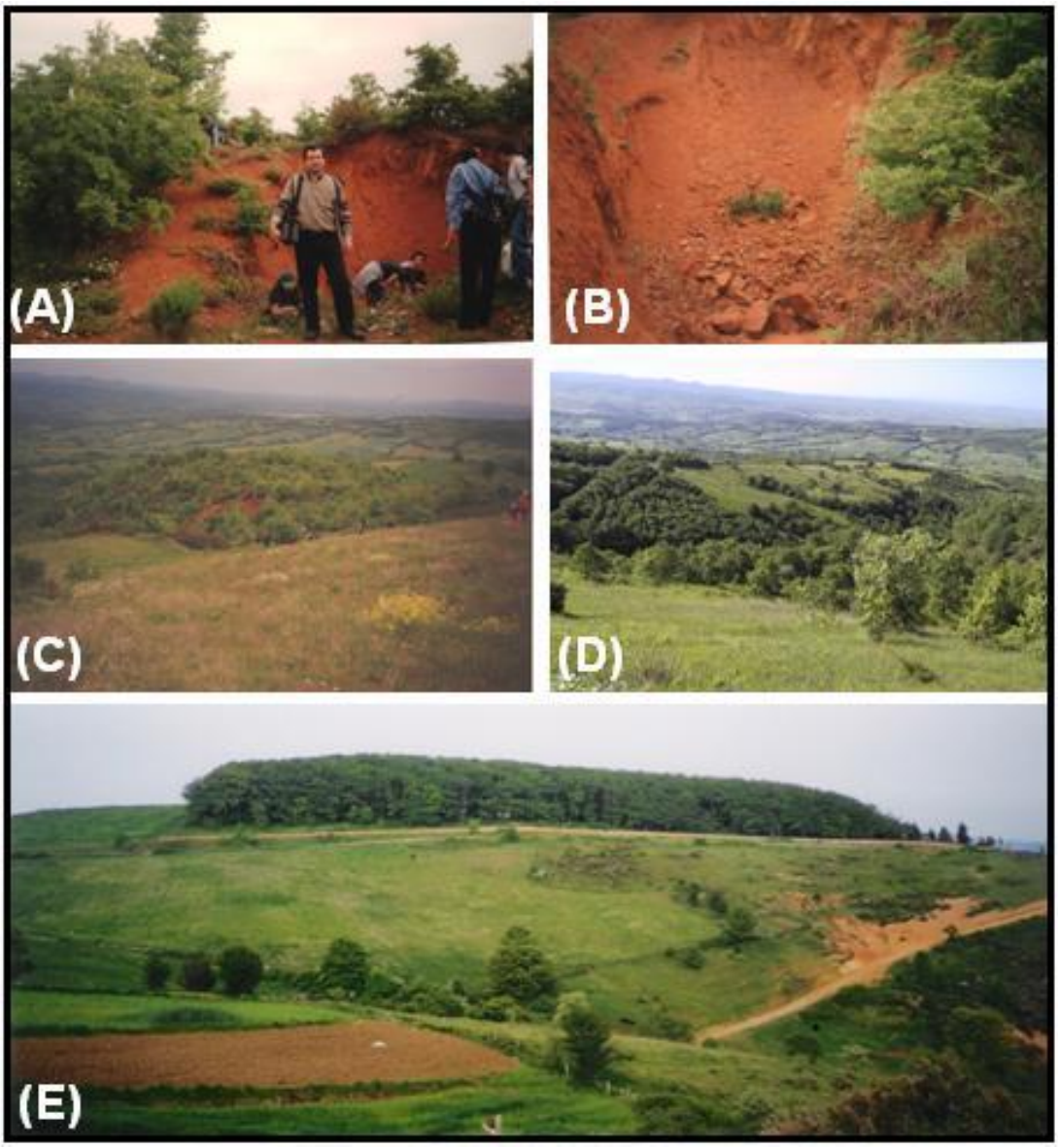

Figure 1.3 Chrysoprase mine field images surrounding the village of Dikmen in the Biga–Çanakkale region. The last pit – like an open-pit mine from which Biga chrysoprase is extracted - has been open since the end of the 1980s **(A)** and **(B)**. The landscape views of this last pit **(C)** and **(D)**. The oldest chrysoprase mine field was opened in the Ottoman Period in about the 1700s. Now, the field is covered with a thick forest **(E)**.

1.3 Advantages of a Non-Destructive (Raman) Further Spectroscopical Method in the Case of a Gemstone Characterization

After the Raman effect was firstly predicted by Smekal in 1923, and later observed experimentally by Raman and Krishnan in 1928 (Raman, 1928), FT-Raman spectroscopy and/or Dispersive(Vis)-Raman spectroscopy have been used as important spectroscopic techniques in condensed matter physics and chemistry to study vibrational, rotational, and other low-frequency modes in a system (Deckert et al., 2008; Gucsik, 2009; Vandenabeele, 2010). The frequency wavenumber of the Raman scattering signal is a reflection of the vibration and rotational modes of the molecule (Lewis and Edwards, 2001; Slodczyk and Colomban, 2010; Vandenabeele, 2010). Raman maps are the images generated from spectra recorded at discrete points of the sample (the recording is automated). They show the variation of any fitted parameter (i.e. intensity, width or position of one band) as a function of the point of analysis. If the mapping is regular and sufficiently tight, one gets a ‘‘smart map’’ of the parameter (color or contrast scaling) superimposed with the optical image of the probed area. Raman mapping is suitable for direct Raman imaging, where a large area of the sample is probed all at once and no fitting is required. More precisely, only photons from a narrow spectral domain are sent to the CCD mosaic and each pixel receives those coming from a given area of the investigated sample. The intensity of the signal thus reveals the presence and location of any substance with a strong Raman signal in the selected spectral window (Gouadec and Colomban, 2007; Colomban and Prinsloo, 2009). The main advantages of Raman spectroscopy are its high information content, lack of sample preparation, compatibility with aqueous systems, and non-destructive nature. In addition, the spectrometer is highly suitable for further gemmological investigations of all kinds of gemstones (Bersani and Lottici, 2010; Fan et al., 2009). Thus, dispersive (green laser) confocal micro-Raman spectroscopy (DCμRS) is one well-known method for the characterization and identification of gem-minerals (Wang et al., 1994). Additionally, if required, it can be used to distinguish similar colored materials from each other non-destructively. Thus, DCμRS can be widely applied to the identification and determination of both

basic and inclusion silica building phases in gem-quality microcrystalline quartz varieties including chalcedonic-quartzes (i.e. chrysoprase, blue chalcedony, agates, jasper, onix, and carnelian) and opalline-quartzes (i.e. fire opals, play-of-color opals, common opals, and dentritic opals).

1.4 Advantages of a Destructive (Luminescence) Further Spectroscopical Method in the Case of a Gemstone Characterization

What causes luminescence is a radiation which is emitted when an electron in the structure falls from a high energy level to a lower one. If the crystal dissipates some of the energy as heat, the radiation emitted has a lower energy than the radiation absorbed. Hence the crystal emits light (Blasse and Grabmaier, 1994; Gaft, 2005; Handerson and Imbusch, 2006). Therefore, it can be summarized that (1) a luminescence encodes the defects that exist in all solid materials, (2) all kinds of minerals show many different types of luminescence relating to the many types of defects (chemical impurities and structural imperfections) they contain, (3) changing the excitation and temperature gives us insights into the causes of mineral and/or material luminescence. Firstly, photoluminescence (PL) is the emission of light from a mineral and/or material when excited by ultraviolet beams. Photoluminescence spectroscopy is a non-contact and non-destructive method of probing the electronic structure of materials. In essence, when the light is directed onto a sample, a process called photo-excitation can occur, where it is absorbed. The photo-excitation causes the material to jump to a higher electronic state, and will then release energy, (photons) as it relaxes and returns to back to a lower energy level. The emission of light or luminescence through this process is photoluminescence (Blasse and Grabmaier, 1994; Gaft et al., 2005; Handerson and Imbusch, 2006). PL (UV-ray induced luminescence) investigations can be used to characterize a variety of material parameters. PL spectroscopy provides electrical (as opposed to mechanical) characterization, and it is a selective and extremely sensitive probe of discrete electronic states. Features of the emission spectrum can be used to identify surface, interface, and impurity levels and to gauge alloy disorder and interface roughness.

The intensity of the PL signal provides information on the quality of surfaces and interfaces (Gfroerer, 2000). Secondly, radioluminescence (RL) (X-ray induced luminescence) is a sensitive technique for studying defects in minerals. X-ray radiation penetrates and excites the whole volume of the crystal, forming new luminescence defects. RL is stimulated when the samples are excited with ionizing radiation (mainly X-ray) from a radioactive source (Gaft et al., 2005). One of the most suitable methods is that RL light is detected by a high-sensitivity wavelength multiplexed TL system (Luff and Townsend, 1993). Thirdly, cathodoluminescence (CL) is an optical and electrical phenomenon in which an electron beam is generated by a cathode ray tube, and then impacts on potentially luminescent centres in a material, giving rise to the emission of light. CL (e-ray induced luminescence) provides essential information on provenance, composition, growth fabrics, diagenetic textures, defects in the lattice, and mineral zonation (Marshall, 1988). Peak-width, peak-position, and transition probability of the luminescence centres are influenced by effects such as interactions within the defects themselves, and interaction between defects and the surrounding crystal lattice. The actual CL color is determined by the number and type of emission and quenching centers present. Superposition of several luminescence bands of different intensities can provide quantitative data on the wavelength and intensity of luminescence and the nature of the luminescence centers (Götze, 2000; Townsend and Rowlands, 2000; Habermann, 2002). Finally, thermoluminescence (TL) glow curves which are created by a heat process have a great importance in identifying the extent of utility of the material to be used in measuring radiation doses (Melo et al., 2004).

These analytical methods approach in a non-destructive and non-invasive way during the investigation of a gemstone sample by simply focusing the scope objective focal point to different depths in the sample. Therefore, especially micro-Raman spectroscopy was introduced into the gemmology field in the late twentieth century. Moreover, it is becoming more and more important in mineral research, and many related applications have been reported by many researchers (Gendron and Smith, 2002; Fan et al., 2009). Thus, it can be stated that dispersive confocal micro-

Raman spectroscopy (DCμRS) is a well-known method for the analysis of gem-minerals. However, DCμRS has not yet been widely used for the identification and determination of Biga chrysoprase.

1.5 Aims and Scope

It has been stated by many authors that the massive-structured green chalcedonic quartz (chrysoprase) material can be confused with the massive-structured green-stained opalline quartz and crystalline quartz materials (Arem, 1987; Shigley et al., 2009), since many chrysoprase-bearing serpantinitic deposits in the world can contain a mixture of prasopal, green-stained quartz, and other nickel- and magnesium-rich minerals (Caillaud et al., 2009; Shigley et al., 2009). Therefore, it is still an important problem to distinguish these similar colored silica varieties non-destructively in the gem market.

This study aims (1) to reveal the geological formation conditions of Biga chrysoprase gemstone, (2) to fully characterize Biga chrysoprase, using several non-destructive and destructive basic and further analytical methods, (3) using the dispersive (green laser) confocal micro-Raman vibrational bands of Biga chrysoprase as the best modern non-destructive method, to distinguish clearly the chalcedonic-quartz silica building phase (fibrous quartz (length-fast chalcedony)), which is the main chrysoprase forming silica phase, from the crystalline-quartz silica phase (fine-grained alpha-quartz) in the case of both quartz inclusions in the green-colored chrysoprase material and of the green-stained quartz material itself in the same deposit, and (4) using the three different luminescence excitation spectra of Biga chrysoprase as the best modern destructive method, to reveal individual luminescence reactions when excited with various irradiaitions, relating to its chemical impurity implications.

CHAPTER TWO
MATERIALS AND METHODS

2.1 Materials

The investigated chrysoprase samples were obtained from the chrysoprase pit near the village of Dikmen, in the district of Biga in the province of Çanakkale (Turkey). The dimensions of the chrysoprase roughs occurring as fracture fillings vary in size from small (about 1 cm in thickness) to giant (about 50 cm in thickness) according to the size of the minor cracks in the deposit.

2.2 Instrumental Methods

In order to verify that Biga chrysoprase samples were indeed a silica (SiO_2) variety, some basic gemmological (non-destructive) characterization tests were carried out on the many representative samples (Table 2.1). The tests were performed in the DGL Gemmological Testing Laboratory of Dokuz Eylül University.

Firstly, the average specific gravity (SG) values of the eight representative samples were measured using an electronic balance scale (measurement sensitivity of 0.001) with an SG kit, based on the formula (SG = Wair/Wair - Wwater) (Figure 2.1). The specific gravity values were obtained in the range between 2.52 and 2.58.

Secondly, because Biga chrysoprase is translucent and opaque, the optical character, optical sign, and refractive index values of the eight representative samples were determined by the "spot" method, using an Eickhorst SR/XS standard refractometer device with an optical contact liquid of 1.79 RI, and a quartz lamp with a wavelength of 589 nm (Figure 2.2). The analysis shows that the samples are anisotropic, uniaxial, positive (+), and their refractive indexes (RI) are Nω = 1.54 and Nε = 1.55; also, the double refraction (DR) is 0.010.

Thirdly, ultraviolet (UV) photo-luminescence reactions of the eight representative samples were observed using a System Eickhorst UV 240 shortwave (255 nm) and long wave (366 nm) 4W UV lamp (Figure 2.3).

It was found that, the samples are inert against UV beams. Thus, especially when the average specific gravity value of 2.55 is considered, as well as the other verifying results, it is indicated that the investigated chrysoprase samples have a typical microcrystalline structure with pores (called chalcedonic-quartz), since the gem quartz varieties with a macrocrystalline structure without pores (called crystalline-quartz) (i.e. amethyst, rock crystal, citrine, etc.) have a specific gravity value of about 2.65 (Back and Mandarino, 2008; Rossman, 1994; Arem, 1987).

Table 2.1 Some gemmological data of the Biga chrysoprase from Turkey regarding to the refractive indexes (RI), specific gravity (SG) values, and UV fluorescence reactions.

Basic gemmological data	**Biga Chrysoprase**
Specific Gravity (SG)	Range of 2.52-2.58 Average= 2.55
Refractive Index (RI)	Nω=1.54 and Nε=1.55
Photo-Luminescence against UV excitation	Inert

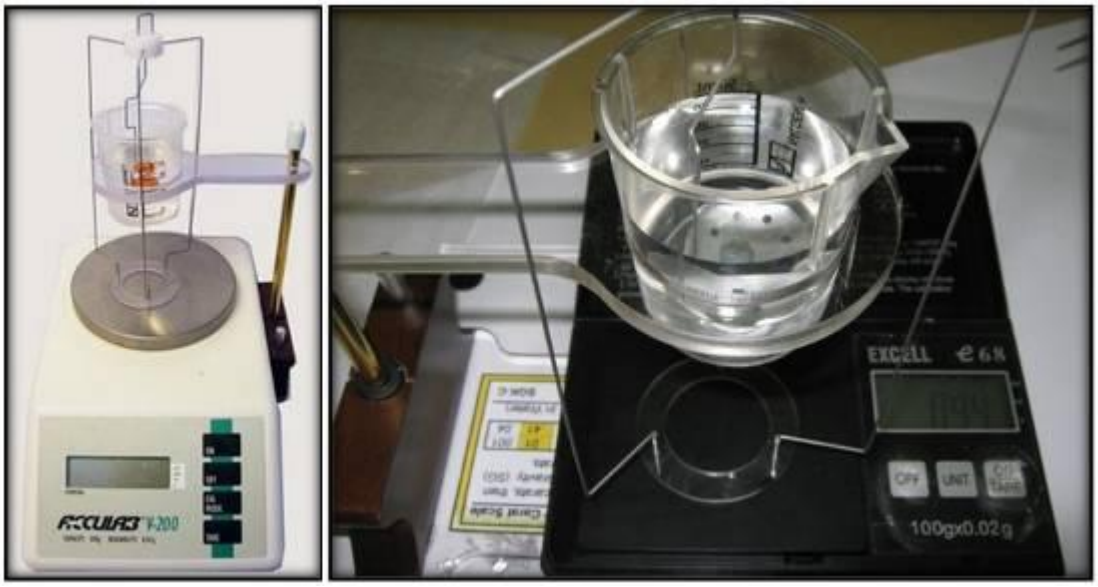

Figure 2.1 Gemmological specific gravity apparatus for sensitive measurement of the weight in air and the weight in water of Biga chrysoprase.

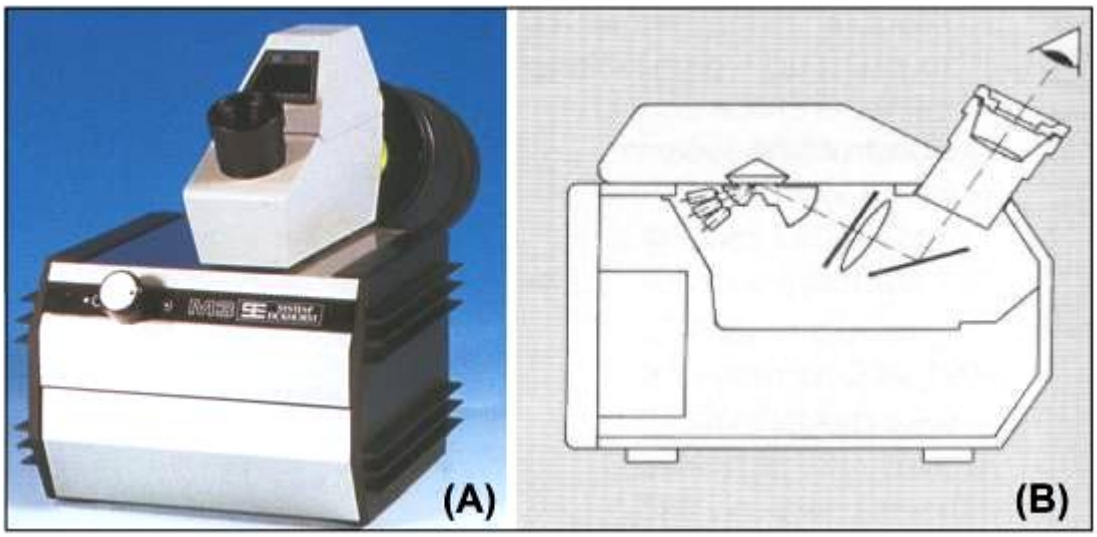

Figure 2.2 Perspective **(A)** and longitual section **(B)** images of the gemmological standard refractometre device used for measuring the refractive index values of Biga chrysoprase, including optical character and optical sign with an optical contact liquid of 1.79 RI, and a quartz lamp with a wavelength of 589 nm.



Figure 2.3 Gemmological ultraviolet lamps for measuring the long and short photo-luminescence reactions of Biga chrysoprase.

In order to verify that the investigated chrysoprase samples were indeed a microcrystalline silica variety (called chalcedonic-quartz), some basic mineralogical (destructive) characterization tests were carried out on the many representative samples.

Firstly, polarizing microscope images of thin sections of Biga chrysoprase were obtained using an Olympus BX41 binocular polarizing microscope with a high intensity 6V, 30W halogen light source combined with U-CPA and U-OPA optical systems, after thin sections of the samples had been mounted on glass lamellae (Figure 2.4). For the digital images, the microscopic magnifications (MM) are as follows; 4X (a combined magnification of 0.4X objective and 10X ocular) and 10X (a combined magnification of 1X objective and 10X ocular) under crossed nicols (+N) (active polarizer and analyzer). The polarizing microscope investigations were performed in the Optical Mineralogy Laboratory of the Department of Geology at Dokuz Eylül University.

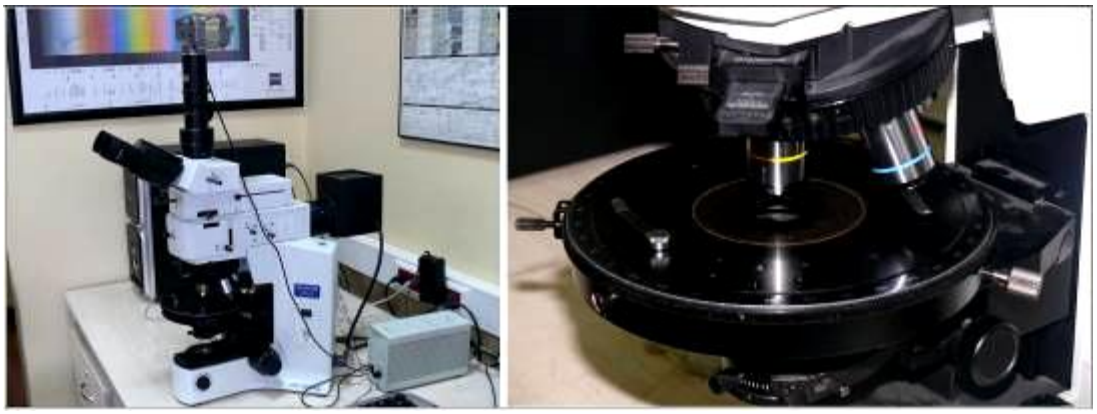

Figure 2.4 Olympus BX41 binocular polarizing microscope with a high intensity 6V, 30W halogen light source combined with U-CPA and U-OPA optical systems, used in this investigation.

Secondly, the base silica building components of Biga chrysoprase were detected from X-ray powder diffraction patterns made using a Cubi-XRD device with a Cu tube and a graphic monochromotor. The samples were analyzed with Cu radiation and a 0.3 mm collimator at atmospheric pressure for 10 min each, in the range between 5 and 70° 2-theta. The d-spacing [A^{o}] diffraction matchings using the comparative matching technique are based on the positions of peaks with relative intensities [%(I/Io)≥2], 2-theta values below 70°, and a tolerance range of ±0.01. X-ray diffraction patterns were recorded in the Material Research Laboratory of the Batı Anadolu Cement Factory in İzmir.

Thirdly, the infrared (IR) pattern of Biga chrysoprase was recorded on a Perkin-Elmas Infrared spectrophotometer in the wavelength range of 200-4000 cm^{-1}, using the KBr pellet technique. The spectrum was obtained in the Department of Chemical Engineering of Ege University in İzmir.

In order to certify the investigated chrysoprase samples, some further mineralogical (destructive and non-destructive) characterization methods were carried out on the many representative samples.

Firstly, chemical analysis of Biga chrysoprase utilized X-ray fluorescence (XRF) for major oxides, inductively coupled plasma-atomic emission spectroscopy (ICP-AES) for trace elements, and WST-SIM for determination of ignition losses. These

analysis was performed, and certified with the code number ‘‘IZ10048288’’, under contract by the accredited ALS Chemex Laboratory in Canada.

Secondly, the dispersive confocal micro-Raman spectroscopy of Biga chrysoprase was performed on a dark background at room temperature using a HORIBA Jobin Yvon Scientific XPLORA dispersive confocal micro-Raman spectrometer (DCμRS) with a high throughput integrated spectrograph (Figure 2.5). The spectrometer uses one laser excitation of about 532 nm (green light). Spectral manipulation as baseline adjustment was carried out using the software of the device. The Raman record was obtained in the DGL-Gemmological Testing Laboratory of Dokuz Eylül University in İzmir.

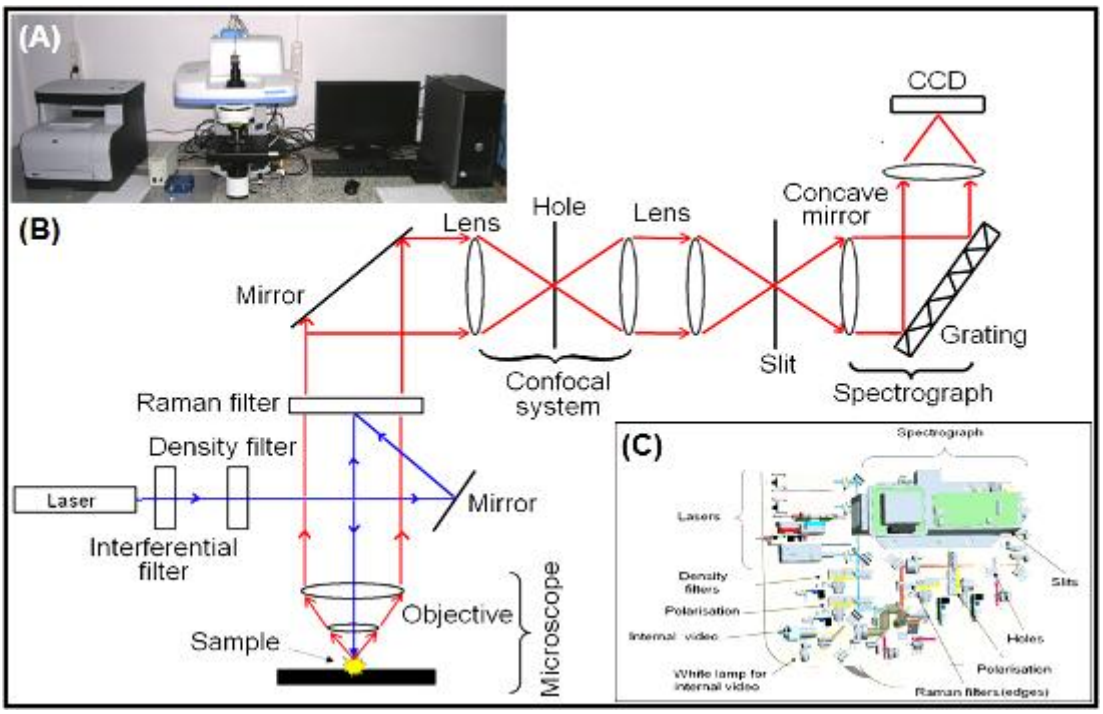

Figure 2.5 The dispersive confocal micro-Raman spectrometer used in this study **(A),** its schematic diagram **(B)** and description **(C)**.

Thirdly, the optical absorption spectrum (OA) of Biga chryoprase was recorded using Varian DMS 90 UV/VIS and Sosco Model 7800 UV/VIS Spectrophotometers in the range of 200-800 nm.

Fourthly, photoluminescence (3D-PL) morphology of Biga chrysoprase was obtained using a Fluorolog 2T Fluorescence Spectrometer. A Xe-lamp with a wavelength range of approximately 370 to 850 nm and a temperature range of approximately 230 to 330 K was used as excitation. Luminescence can either be after excitation (where the primary beam has higher energy than the secondary light) or stimulation (where the primary beam has less energy than the luminescence). These wavelengths were selected using a monochromator (Spex 1681 0.22 mm) and emission analysed with a Spex 1680 Double Spectrometer. The detector is a front-illuminated open-electrode CCD (200-1100 nm). Finally, the photoluminescence (3D-PL) images of the samples were originally taken using Axum 5.0 software. Later, the 3D-PL morphology was converted into a 2D-PL counter map as using Surfer 8.0 software. Next, many 2D-PL graphics were produced from the 3D-PL morphology using Surfer 8.0 and Grapher 8.4 software.

Fifthly, cathodoluminescence time resolved spectroscopy was performed on Biga chrysoprase samples. The current was 20 mA. The acceleration potential was the energies of 14 and 24 keV electrons corresponding to an incident power density of 0.8 μAcm^{-2} at room temperature. The primary electron beam is normally pulsed using a Thandor TG501 5 MHz function generator as a function with the frequencies of 90, 180, 360, and 900 Hz at 14 keV, and with the frequencies of 90, 180, 360, 900, and 9000 Hz at 24 keV, except for the lifetime measurement. The CL response was gated using an EgandG Ortholoc-SC 9505 2-phase lock-in amplifier, and a cooled red-sensitive photomultiplier tube. It is worth noting that the broad diameter of the beam significantly reduces any instability due to secondary electron emission. The light coming from the samples was focused via a quartz lens onto the entrance slit of a grating monochromator with f/4 light collection, and detected with a blue-sensitive photomultiplier tube (PMT, EMI 9813Q). The quantum efficiency of EMI 9813Q is between 15% and 25% in the range of 250 nm to 800 nm. Two different measurements can be performed on the samples, using the alternating current (AC) and the direct current (DC) generated in the system. DC measurements can potentially record optical signals from the electron gun source, but this is rejected in the AC operating mode. However, only Alternating Current (AC) measurements

were used on the samples at room temperature during the experiment. In AC measurement, an Ortholoc-SC9505 two phase lock-in amplifier was employed. This instrument was used in normal mode where it performs in exactly the same way as an ordinary lock-in amplifier, i.e. only one channel is needed. The spectral lines obtained using a mercury (Hg) discharge lamp and Nd:YAG laser were used in wavelength calibration using 3 mm entrance and exit slits on the monochromator. The wavelengths of the spectral lines used in the calibration are 405, 436, 546 and 577 nm for the Hg and 633 nm for the He-Ne laser. The efficiency of the spectral response of the whole system was obtained by recording the spectrum of a tungsten lamp used with the same aperture as in the wavelength calibration. Hence it was possible to correct the wavelength dependent sensitivity of the system. The electron beams were chopped at frequencies from 9 to 900 Hz, and the photomultiplier output was measured on a lock-in amplifier. The wavelength resolution was set at 5 nm for the CL measurements. Due to changes in ion beam energy, the current density may modify the emission spectra and intensity.

Finally, the thermoluminescence (TL) glow curve of Biga chryoprase was recorded using a computer controlled thermoluminescence dosimeter reader Harshaw 3500 with a linear heating rate of 2 Cs^{-1} in N_2 atmosphere at temperatures ranging from 50 to 400 ^{o}C. The samples were first irradiated with X-ray at room temperature for 5 minutes using a Norelco tungsten X-ray tube (Machlett OEG-50A) working at 30kV, 15mA, in order to facilitate the thermoluminescence light output. The filter used was a Schott KG1, and the measurements were taken immediately after irradiation under red light in order to overcome any fading effects which influence glow curves.

CHAPTER THREE
RESULTS AND DISCUSSION

3.1 Provenance and Genesis of Biga Chryoprase

Regarding mining, during the field investigation, it was seen that the large and small chrysoprase pits near the Dikmen village of Biga have been well-preserved from the past to now (Figure 1.3).

Regarding geology, on the large scale, the Biga Peninsula comprising the whole Biga–Çanakkale region as well as the village of Dikmen, which is near the chrysoprase depositional field, is geologically described in detail by some authors (Bingöl et al., 1973; Okay et al., 1991; Okay and Satır, 2000; Koçyiğit et al., 2006). Significantly, it has been reported that there is a major NE–SW trending tectonic belt running from the district of Karabiga to the district of Ezine, which characterizes the region. In addition, it is seen that the chrysoprase bearing zone in the region is on this tectonic belt. The Biga Peninsula comprising the whole Biga–Çanakkale region as well as the village of Dikmen, which is near the current chrysoprase depositional field, is an active deformational area bounded by the northern Aegean Sea to the west, the Dardanelles to the northwest, the Sea of Marmara to the north, the Gulf of Edremit to the southwest and the Havran–Manyas line to the east-southeast. Therefore, the Peninsula is a tectonically very active area included in the central-northern Aegean strike-slip neotectonic domain in which the principal compressive stress is operating in approximately an E–W direction (Koçyiğit et al., 2006).

In the Aegean region, the closure of the northern Neotethyan Ocean, an ongoing compressional regime, and subsequent crustal thickening occurred from the Late Cretaceous to the Palaeocene and have resulted in the amalgamation of various tectonic units (Figure 3.1).

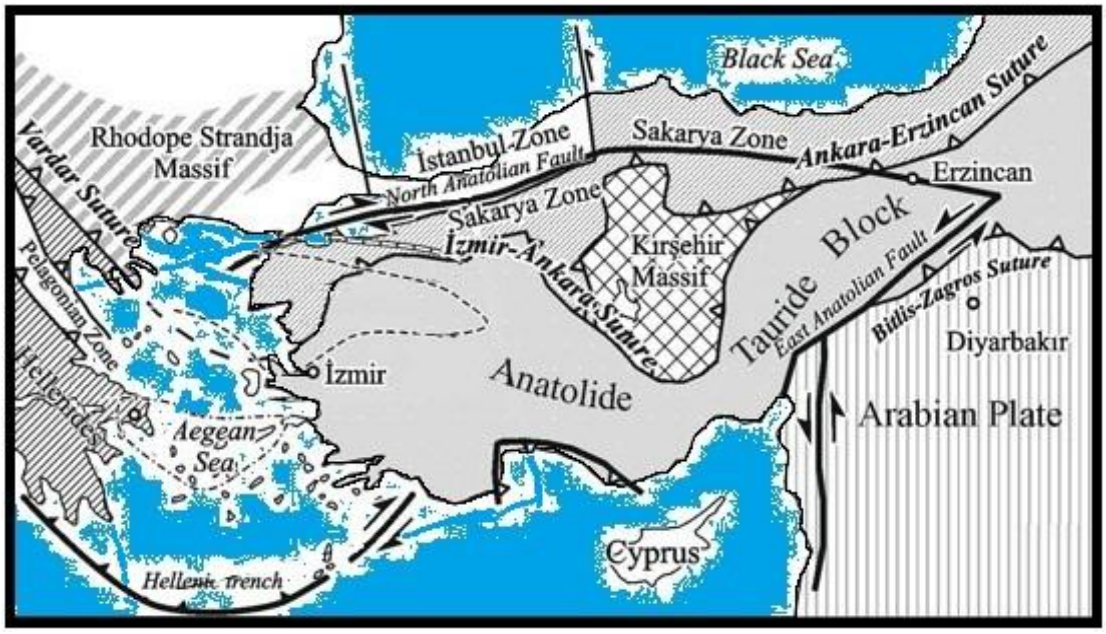

Figure 3.1 Location and tectonic map showing the position of the major faults present on Anatolian land and under the Aegean and Mediterranean Seas (modified after Okay et al., 1991; Okay and Satır, 2000; Koçyiğit et al., 2006).

In addition, medium-grade metamorphic rocks crop out over a large area under the Neogene sedimentary and volcanic rocks in the central Biga Peninsula in northwest Turkey (Okay and Satır, 2000). It can be seen that the chrysoprase bearing zone within the ultrabasic-characterized serpentinites at the contact border of the metamorphic schists in the region is on this tectonic belt. Therefore, chrysoprase materials are mainly found as fracture fillings covered with a weathering crust in the silicified serpentinites (Figure 3.2).

As a result of the detailed field investigation, it can be stated that the chrysoprase material in the Biga–Çanakkale region (Turkey) occur due to precipitation of silicic acid-rich dissolutions (H_4SiO_4) circulating through several fracture zones under ambient surrounding conditions -similar to those of the worldwide localities (Komov et al., 1994; Skrzypek et al., 2003 and 2004). However, the silicic acid-rich dissolutions were firstly precipitated as the chalcedonic-quartz base silica phase [fibrous quartz (lengthfast chalcedony)] throughout the outer edges of the open fractures. After that, the remaining dissolutions in the central parts of the fractures were coagulated as both the chalcedonic-quartz interval silica phase (fibrous length-

slow moganite) and the crystallinequartz silica base phase (fine-grained alpha-quartz) as inclusions depending on the temperature rise of the dissolution (Frondel, 1978; Miehe and Graetsch, 1992; Murashov and Svishchev, 1998).

Similar chrysoprase formations have been reported in many previously published papers. Accordingly, it is widely stated that the chrysoprase material can occur upon liquid–solid interactions under ambient conditions (Nagase et al., 1997; Sachanbinski et al., 2001; Skrzypek et al., 2003 and 2004; Witkowski and Zabinski, 2004; Befi, 2009; Shigley et al., 2009). The trace element contents of the chrysoprases are associated with the serpentinized and silicified nickel- and magnesium-rich ultrabasites (Komov et al., 1994). Additionally, during chrysoprase occurrence, mainly nickel, iron, and magnesium elements enter the silica-rich dissolution, and then migrate together with the dissolution. Finally, the independent mineral phases of nickel and nickel-magnesium hydrous silicates occur at a PH of about 6–7 (Komov et al., 1994). The most complete profiles are usually present over the weathered serpentinites, while on top of the less altered pyroxenites, there only usually exist the formation of a limonitic zone (Caillaud et al., 2009). Skrzypek and his colleagues (2004) stated that the chrysoprase samples analyzed from Poland, Kazakhstan, and Australia were formed in veins, and they were apparently associated with somewhat younger vein magnesite. In addition, their high oxygen isotope ratios suggested that the chrysoprase was precipitated from mixed meteoric solutions in hydrothermal conditions (Skrzypek et al., 2004).

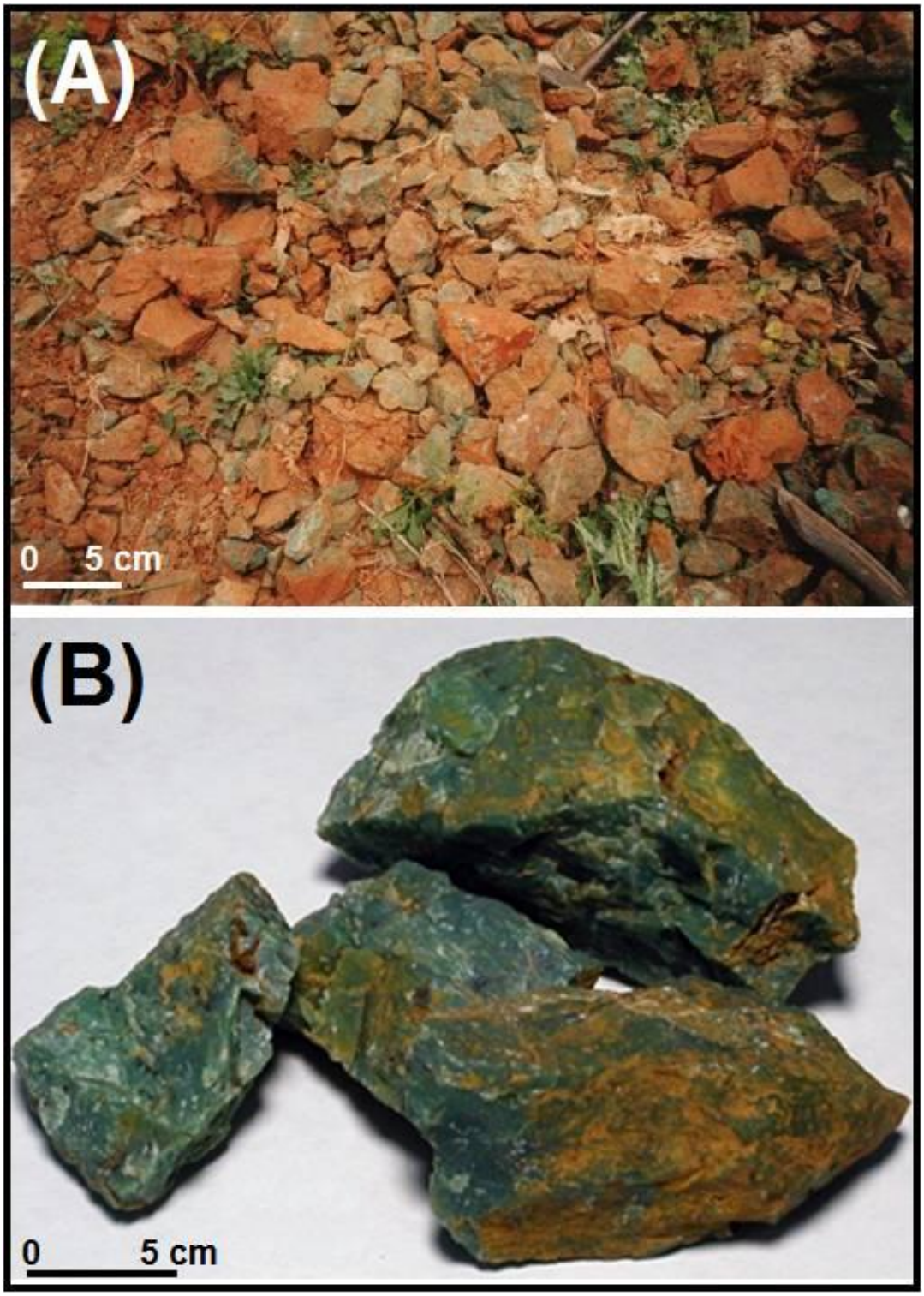

Figure 3.2 Gem-quality dark green chrysoprase roughs are found as the fracture fillings in the silicified serpentinite cracks throughout the border of the metamorphic zone. The dimensions of the samples occurring as fracture fillings vary according to the size of the cracks **(A)**. Thus, they are massive structured irregular masses covered with a weathering crust, which vary in size from small (about 1 cm in thickness) to giant (about 50 cm in thickness) **(B)**.

3.2 Lapidary

Some of the chrysoprase samples collected from the Biga mine field (Figure 3.2) were cut and polished into cabochons and slabs as gem objects to show its typical color and gem quality. It can be seen that the polished objects display the individual green color and good quality of the chrysoprase material (Figures 3.3 and 3.4).



Figure 3.3 Polished block **(A)** and rough slab **(B)** samples of Biga chrysoprase.



Figure 3.4 Some polished cabochon samples of Biga chrysoprase to show its typical color and gem quality.

A Biga chrysoprase rough piece (Figure 3.5A) was sectioned into parts small enough to be cut further by other lapidary processes (Figure 3.5B). For this purpose, several types of diamond saw blades were used, each mounted in appropriate machinery, depending on how large the chrysoprase rough was and exactly what would be done to it. In the case of irregular bits of rough, such as pebbles and broken fragments, great care was taken to prevent them from tilting and grabbing the blade.

Then, cabochon cutting of Biga chrysoprase is began. However, before this process, it was necessary to obtain several excellent plastic templates with openings of a standard size. Lead pencils are not much good for marking the stone. Instead, metal wires or rods are much better. While the chrysoprase slabs were being marked, it was necessary to lay the template flat, insert the sharp point of the metal pencil into the opening, and run it along the inner edge (Figure 3.5C). Next, the marked slab was trim sawed to cut away the cabochon blanks (Figure 3.5D). Finally, the blanks were further sawed to remove large projections, leaving the inscribed outline surrounded by a series of flat cuts. Then, the nibbling process was applied to the stone (Figure 3.5D). Stones that could not be nibbled had to be ground to shape. Because the trim saw makes only straight cuts, the blank is surrounded by triangular projections of waste stone. Instead of grinding these away, a pair of pliers is used to break off or nibble the useless points.

After nibbling, the stone was ready for grinding to make a cabochon form. However, before this process, the stone was dopped on a dipstick for easier handling. Sealing wax and stick shellac are used to make dopping wax. A good bond between the stone and wax requires that both be hot; a cool joint will break during grinding. While the wax was still tacky, the stone was carefully centred on the top, reheating as necessary to keep the wax pliable. After the stone had been dopped and readjusted to sit squarely on the dipstick, it was set aside to cool.

Then, rough grinding the top was begun for cabochon cutting (Figures 3.5E and 3.5F). The first step in grinding the top was to put a broad level around the edge, sloping from the bottom toward the top. Since a vertical wheel was used, the

procedure was as follows: Hold the dop in the fingers of the left hand, close to the base of the cabochon. The aim is to make the first bevelling cut to full depth, repeating until the bevel reaches the base of the cabochon. After the bevel is cut, another cut is made along the top. Once the top is covered with concentric bevels, the basic form is established. The outline is preserved, the bevel evenly cut, and the top smoothly curved with no flat spot.

After the basic cabochon form was given to the stone, the surface was smoothed to prepare it for sanding. The purpose of wet sanding on a cloth is to smooth and not to shape. Belt senders made of silicon carbide (SiC) provide a slack area between rollers where the cloth curves around the stone and promotes rounding (Figure 3.5G). By selecting the proper spot, every degree of curvature and stiffness of surface can be had. When fine sanding has been completed, the stone's surface should show an excellent glossy finish, covered with a multitude of minute scratches.

The final step of cabochon cutting is polishing. As in grinding and sanding, it is necessary to adopt a routine for completing the stone. Firstly, a vertical buff is installed and wet thoroughly (Figure 3.5H). After the buff is damp, the powder solution is applied with a small brush, dipping from the pot with a stirring motion. Well-sanded cabochon samples polish easily, but if the polish is dull or pitted, a switch should be made to a leather or wood buff.

The finished stone was cleaned off with alcohol to remove wax (Figure 3.5J). If polishing powder has worked its way into crevices, brisk scrubbing with soap and water may remove it.

Ultimately, chrysoprase gems cut and polished in standard cabochon form can be mounted on rings and earrings (Figure 3.6).



Figure 3.5 Gemmological (lapidary) study of Biga chrysoprase to show its typical color and gem quality.



Figure 3.6 Gemmological (jewellery) study of Biga chrysoprase.

3.3 Polarizing Microscopy (PM)

Investigations of thin sections at magnifications of 2X, 4X, and 10X under a polarizing microscope revealed that Biga chrysoprase consists mainly of micro-crystalline fibrous and fine-grained matrix materials (Figures 3.7, 3.8, and 3.9). Even though the major portion of the chrysoprase matrix contains fibrous radial and/or bundled particles of the chalcedony silica phase (fibrous quartz, optically length-fast) signing the chalcedonic-quartz silica building phase (Frondel, 1978; Miehe et al., 1984), the, minor portion of the chrysoprase matrix contains centrally located inclusions with fine-grained particles of the alpha-quartz silica phase (fine-grained quartz, optically length-fast) and fibrous radial and/or bundled particles of the moganite silica phase [fibrous moganite (or lutecite, or quartzine), optically length-slow] (Miehe and Graetsch, 1992; Murashov and Svishchev, 1998). However, the fine-grained particles of the opal-CT and opal-C silica phases signing the opalline-quartz silica building phases were not observed in the Biga chrysoprase matrix; thus it can be stated that Biga chrysoprase occurs at relatively higher (over 80–90 ^{o}C) formation temperatures than in other localities worldwide (Skrzypek et al., 2004).

On the other hand, in the chrysoprases found in other locations of the world, the opalline-quartz silica building phases have been identified and reported rather than moganite. Accordingly, three mineralogical silica building phases were specified in the chrysoprases from Poland: (a) opal phases (opal-CT and opal-C)–the opal matrix

contains chalcedony or quartz crystals; (b) chalcedony phase–microcrystal or fine-crystal structure, (c) chalcedony–opal phase (continuous structural transition from chalcedony crystals to quartz crystals) (Sachanbinski et al., 2001; Skrzypek et al., 2003 and 2004). The silica phases in the chrysoprases from Kazakhstan have been identified as being similar to that of the chrysoprase from Poland (Sachanbinski et al., 2001; Skrzypek et al., 2003 and 2004). The structure of the chrysoprase from Australia was divided into two different groups: (a) the dominant onemicrocrystal quartz and fibrous chalcedony and (b) the second type: crystals of chalcedony and quartz surrounded by an opal matrix (Nagase et al., 1997; Skrzypek et al., 2004; Befi, 2009).

As a result, because of the existence of the chalcedonic-quartz silica interval phase (moganite) instead of the opalline-quartz silica base phase (opal-CT and opal-C), it can be stated that the Biga chrysoprases occur at relatively higher formation temperature conditions.

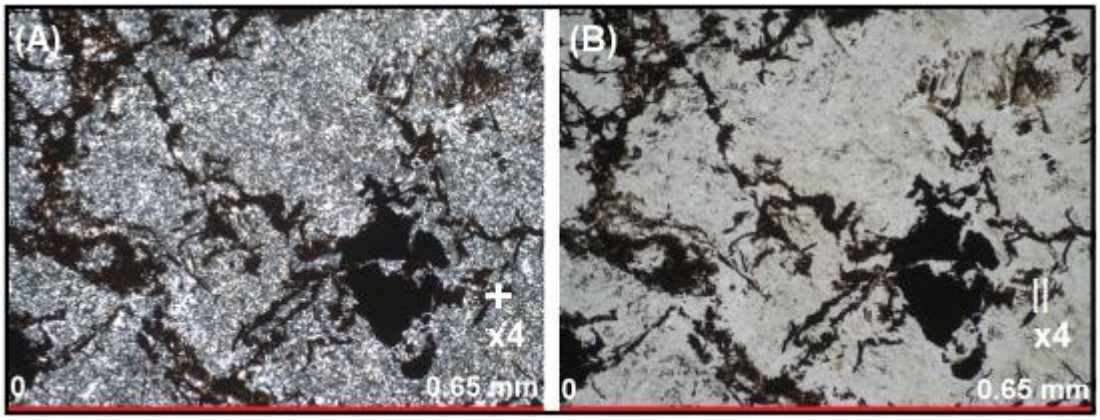

Figure 3.7 Microphographs of Biga chrysoprase, viewed in crossed-polarized light at magnifications of 4X **(A)** and 10X **(B)**. The width of the images is 0.65 mm.

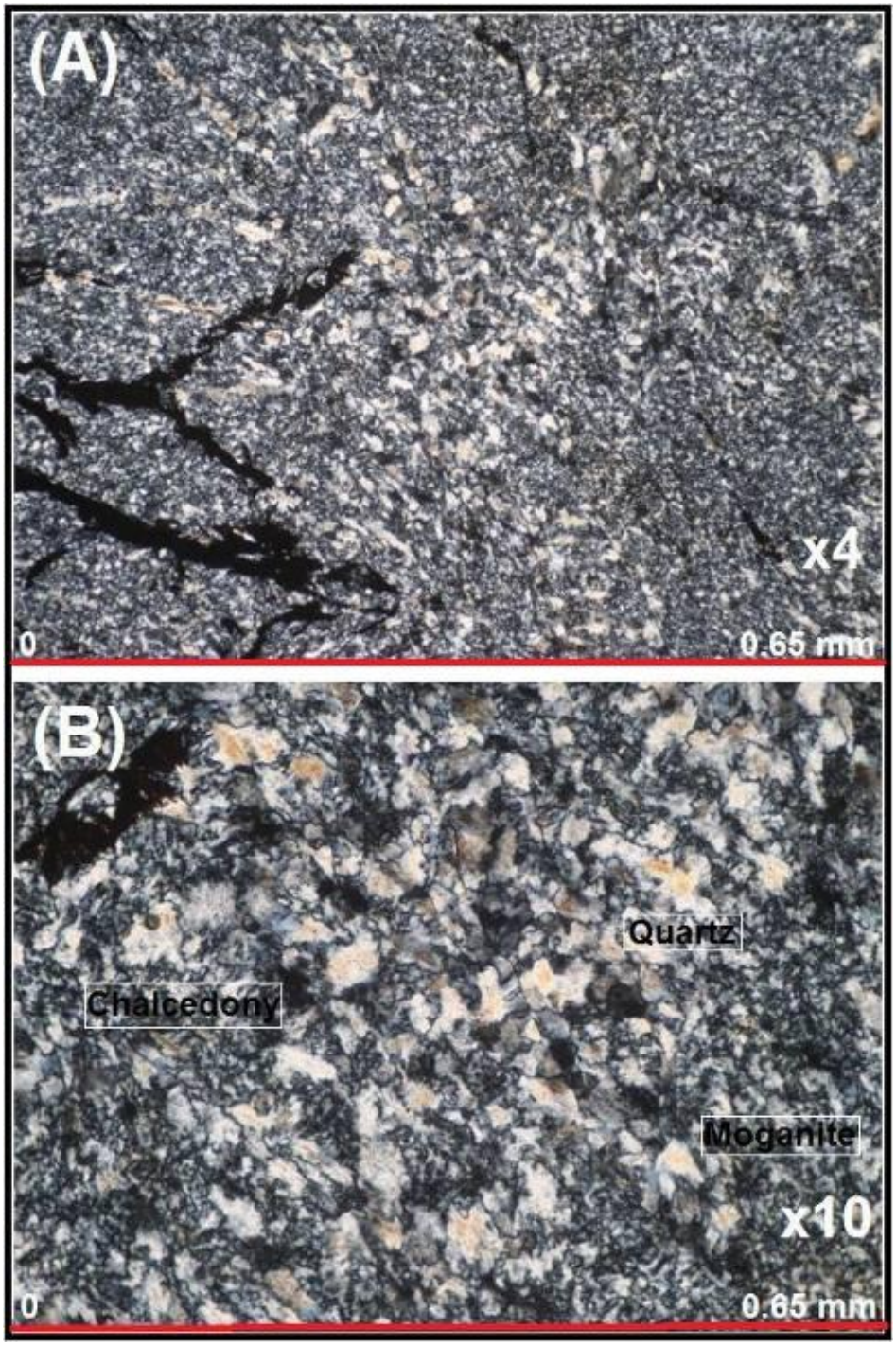

Figure 3.8 Microphographs of Biga chrysoprase, viewed in crossed-polarized light at magnifications of 4X **(A)** and 10X **(B)**. It can be seen that at least 90% of the massive chrysoprase mass consists of the fine radial fibrous chalcedony silica building phase with length-fast undulation (chalcedonic-quartz). The remainders were crystallized with a fine-grained alpha-quartz silica phase with length-fast undulation, and a fine radial fibrous interval moganite (or lutecite) silica phase with length-slow undulation. The width of the images is 0.65 mm.

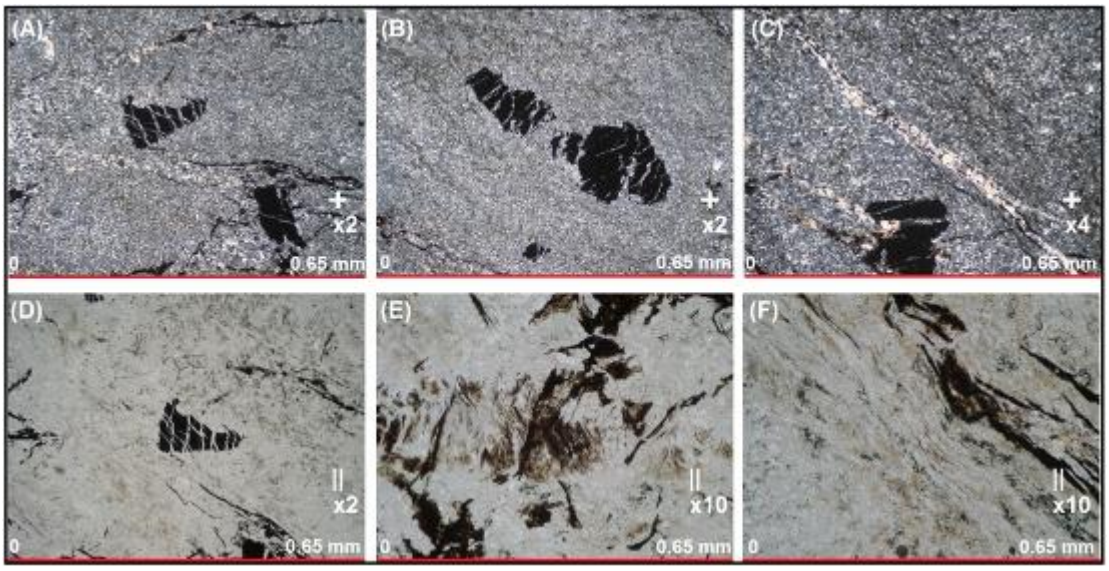

Figure 3.9 Microphographs of Biga chrysoprase, viewed in crossed-polarized light at magnifications of 2X **(A)(B)(D)**, 4X **(C)** and 10X **(E)(F)**. The width of the images is 0.65 mm.

3.4 X-Ray Diffractometry (XRD)

Table 3.1 shows the identification of the three different silica phases present in Biga chrysoprase, which evidence the temperature conditions during the formation of the silica. Accordingly, in order to verify the silica building phases in the Biga chrysoprase matrix, the numerical data obtained from the XRD analyses of the representative Biga chrysoprase samples were matched to those of ideal crystalline-quartz, chalcedonic-quartz, and opalline-quartz silica building phases, using a comparative matching technique using values compiled from some important crystal structure databases (AMCSD, 2012; RRUFF, 2012; WEBMINERAL, 2012) and PDF cards (ASTM, 1963) as well as some previously published related papers (Miehe et al., 1984; Miehe and Graetsch, 1992; Murashov and Svishchev, 1998). The matched silica phases were labeled with specific abbreviations to help the readers as (Qu) for alpha-quartz, (Ch) for chalcedony, and (Mo) for moganite on the given X-ray diffraction pattern (Figure 3.10). However, the main chalcedonic-quartz silica phase (fibrous chalcedony) could not be clearly distinguished from the main crystalline-quartz silica phase (fine-grained alpha-quartz), since both exhibit the same numerical XRD data (Smith, 1997; Cady et al., 1998). Therefore, the labels belonging to fibrous chalcedony (Ch) and fine-grained alpha-quartz (Qu) were

labeled on the same peaks (Figure 3.10). As can be seen in the representative XRD pattern, Biga chrysoprase is composed of major fibrous chalcedony and minor fibrous moganite and fine-grained alpha-quartz inclusions (Figure 3.10). The XRD data of Biga chrysoprase show a lack of fine-grained opal-CT and opal-C, which represent the opalline-quartz silica building phases of the microcrystalline quartzes (Jones and Segnit, 1971). This result may suggest silica formation conditions over about 80 ^{o}C. In many previously published papers, it has been stated that chalcedonic-quartz precipitations occur in the range between 40 and 150 ^{o}C. However, in microcrystalline quartz occurrences, the coagulations of the kinds of silica building phases depend on the environmental conditions. At lower temperature conditions below about 80 ^{o}C, opal-CT and opal-C opalline-silica building phases appear dominantly. However, at higher temperature conditions above about 180 ^{o}C, the moganite (or lutecite) interval-silica building phase and alpha-quartz crystalline-silica building phase crystallize (Frondel, 1978; Murashov and Svishchev, 1998; Jones and Segnit, 1971).

Table 3.1 Comparative matching of the data obtained from the representative Biga chrysoprase against the ideal data of the chalcedony (Ch), moganite (Mo), alpha-quartz (Qu), opal-CT (Op-CT), and opal-C (Op-C) silica building phases, using the comparative matching technique according to the d-spacing [Å] and relative intensities [%(I/I_o) ≥2] of the experimental XRD numerical data. Labels are arranged according to their relative intensities. However, the chalcedonic-quartz (fibrous length-fast quartz) and crystalline-quartz (fine-grained length-fast quartz) silica phases are mixed in the XRD numerical data.

Silica Phases [SiO_2]	***XRD data (ideal)**			**XRD data (Chrysoprase)**
	[hkl][Å]	[%(I/I_o) ≥2]	Labels	[Å] [%(I/I_o) ≥2]
Chalcedonic-Quartz Chalcedony (Ch)	[100]	**4.26** (22)	**Ch-Qu-Mo**	**4.27** (20.6)
Trigonal- Trapezohedral	[101]	**3.34** (100)	**Ch-Qu**	**3.35** (100)
Microcrystalline-	[110]	**2.46** (14)	**Ch-Qu**	**2.46** (5.8)
Cryptocrystalline	[102]	**2.28** (10)	**Ch-Qu-Mo**	**2.29** (5.9)
Fibrous, Length-fast	[111]	**2.24** (5)	**Ch-Qu**	**2.24** (2.7)
Main constitutive phase	[200]	**2.13** (12)	**Ch-Qu-Mo**	**2.13** (4.2)
	[201]	**1.98** (5)	**Ch-Qu**	**1.98** (2.7)
Crystalline-Quartz Alpha-Quartz (Qu)	[112]	**1.82** (20)	**Ch-Qu**	**1.82** (5.3)
Trigonal-Trapezohedral	[202]	**1.67** (10)	**Ch-Qu**	**1.67** (2.6)
Crystalline	[211]	**1.54** (10)	**Ch-Qu**	**1.54** (5.3)
Fine-grained, Length-fast	[203]	**1.38** (7)	**Mo-Ch-Qu**	**1.39** (5.1)
Inclusion phase	[301]	**1.37** (10)	**Ch-Qu**	**1.37** (4.7)
Chalcedonic Quartz Moganite (Mo) (or Lutecite)	[110]	**4.45** (13)	**Mo**	----------
Monoclinic- Prismatic	[-101]	**4.38** (7)	**Mo**	----------
Microcrystalline-	[002]	**4.26** (5)	**Ch-Qu-Mo**	**4.27** (20.6)
Cryptocrystalline-Interval	[-121]	**3.39** (50)	**Mo**	----------
Fibrous, Length-slow	[022]	**3.33** (100)	**Mo**	----------
Inclusion phase	[-112]	**3.11** (11)	**Mo**	----------
	[130]	**2.88** (5)	**Mo**	----------
	[-141]	**2.29** (9)	**Ch-Qu-Mo**	**2.29** (5.9)
	[123]	**2.19** (5)	**Mo**	----------
	[004]	**2.13** (5)	**Ch-Qu-Mo**	**2.13** (4.2)
	[-143]	**1.83** (13)	**Mo**	**1.83** (9.0)
	[143]	**1.80** (6)	**Mo**	----------
	[125]	**1.53** (5)	**Mo**	**1.53** (3.0)
	[-244]	**1.41** (5)	**Mo**	----------
	[-262]	**1.39** (7)	**Mo**	**1.39** (3.3)
	[145]	**1.38** (11)	**Mo-Ch-Qu**	**1.38** (5.1)
	[082]	**1.28** (8)	**Mo**	----------
	[280]	**1.18** (8)	**Mo**	----------
Opalline Quartz Opal-CT (Op-CT)	[]	**4.33** (90)	**Op-CT**	----------
Microcrystalline-	[]	**4.12** (100)	**Op-CT**	----------
Pseudocrystalline	[]	**3.82** (50)	**Op-CT**	----------
Coarse-grained, Length-fast sometimes Undulotory-damped				
Opalline Quartz Opal-C (Op-C)	[]	**2.51** (30)	**Op-C**	----------
Microcrystalline-				
Pseudo-crystalline				
Coarse-grained, Length-fast sometimes Undulotory-damped				

***Ideal XRD data compiled from**
-AMCSD, 2012. American Mineralogist crystal structure database by Downs et al. (1993) *via http://www.minsocam.org/MSA/Crystal_Database.html, and http://rruff.geo.arizona.edu/AMS/amcsd.php.*
-WEBMINERAL, 2012. Minerals arranged by X-Ray powder diffraction *via* http://webmineral.com/MySQL/xray.php.
-RRUFF, 2012. Database of Raman spectroscopy, X-ray diffraction and chemistry of minerals *via http://rruff.info/.*
-ASTM, 1963. Index (inorganic) to the powder diffraction file; *ASTM special tech. Pub. 48-M2, Am. Soc. for Test. and Mater, Philadelphia, pp. 244.*-PDF cards-86-1630 (for chalcedony); 46-1045 (for quartz); 38-0360 (for moganite); 38-0448 (for opal).
-Miehe et al., 1984; Miehe and Graetsch, 1992; Murashov and Svishchev, 1998
***The diffraction matching using the comparative matching technique is based on the positions of peaks with intensities equal and greater than 2% for those of the ideal and the positions of peaks with intensities equal and greater than 2% for those of the sample, having 2-theta values below 70 deg., and tolerance range of ±0.01.**

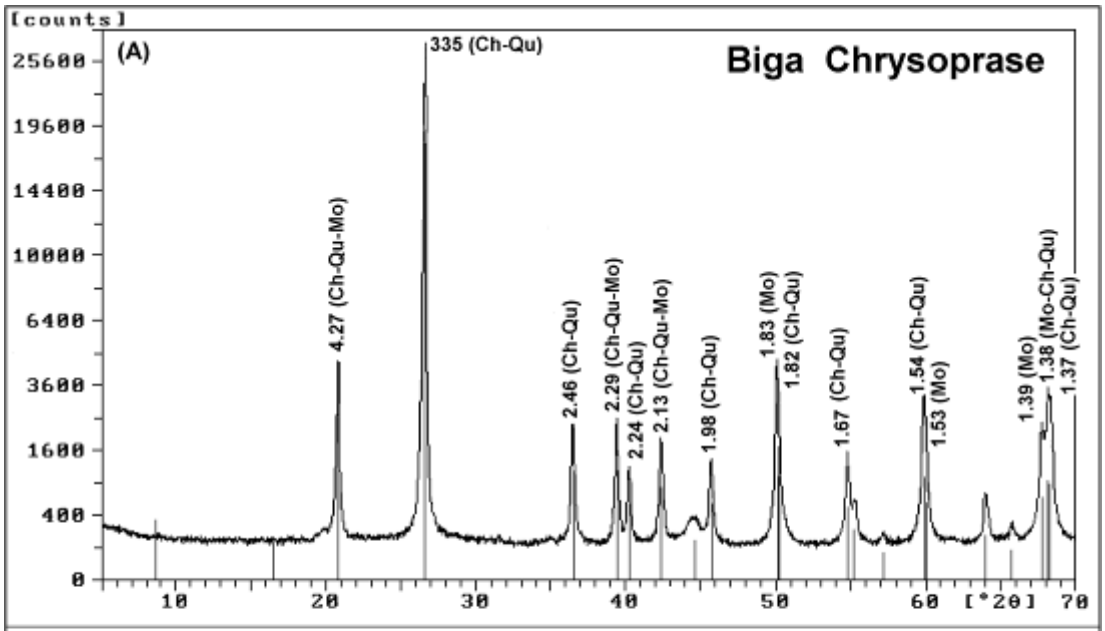

(B)

CUBI-XRD
Sample identification: YO251110
Data measured at: 25-Nov-2010 18:42:00
Tube anode: Cu
Wavelength Alpha1 [Å]: 1.54056
Wavelength Alpha2 [Å]: 1.54439
Start angle [°2θ]: 5.015
End angle [°2θ]: 70.025
Maximum intensity: 17929.21
Intensities converted to: FIXED
Number of peaks: 22

Angle [°2θ]	d-value α1 [Å]	d-value α2 [Å]	Peak width [°2θ]	Peak int [counts]	Back. int [counts]	Rel. int [%]	Signif.
8.700	10.1555	10.1807	0.720	18	335	0.1	0.90
16.500	5.3681	5.3814	0.180	14	154	0.1	0.77
20.830	4.2609	4.2715	0.150	3684	149	20.6	20.86
26.610	3.3471	3.3554	0.180	17929	135	100.0	78.04
36.515	2.4587	2.4648	0.180	1043	71	5.8	17.45
39.430	2.2834	2.2891	0.180	1050	59	5.9	15.37
40.245	2.2390	2.2446	0.210	480	58	2.7	12.83
42.415	2.1293	2.1346	0.180	751	53	4.2	13.35
44.665	2.0272	2.0322	0.240	92	50	0.5	1.39
45.750	1.9816	1.9865	0.210	488	48	2.7	14.26
50.090	1.8196	1.8241	0.150	1616	45	9.0	12.04
50.225	1.8150	1.8195	0.060	955	45	5.3	4.44
54.825	1.6731	1.6773	0.150	467	42	2.6	5.83
55.275	1.6605	1.6647	0.150	199	44	1.1	2.03
57.210	1.6089	1.6129	0.240	24	44	0.1	1.51
59.900	1.5429	1.5467	0.180	949	46	5.3	13.72
60.085	1.5386	1.5424	0.090	529	46	3.0	0.80
63.985	1.4539	1.4575	0.210	149	42	0.8	7.16
65.710	1.4198	1.4234	0.180	42	44	0.2	1.68
67.685	1.3831	1.3866	0.150	600	45	3.3	5.33
68.095	1.3758	1.3792	0.120	906	46	5.1	3.20
68.215	1.3737	1.3771	0.120	847	45	4.7	2.80

Figure 3.10 The XRD pattern of the representative Biga chrysoprase **(A)**, according to the numerical experimental XRD data **(B)**, showing the labels of the single or overlapped peaks of the base microcrystalline and crystalline silica building phase components. These are fibrous chalcedony (optically length-fast) (Ch), fibrous moganite (optically length-slow) (Mo), and fine-grained alpha-quartz (optically length-fast) (Qu). The positions of peaks with d-spacings [Å] and relative intensities [%(I/I_o)] are labelled for ≥ 2% of 2-theta values below 70 degrees. The labels of overlapped peaks are in order of relative intensities [%(I/I_o)].

3.5 Mid-Infrared Spectroscopy (MIRS)

The vibration ranges of the hydroxyl (OH) group water species, main silica mineral building components and/or inclusions, structural point defects, structural bonds, and coloration in silica can be determined using the infrared (IR) pattern in the mid-infrared region (Taylor et al., 1970; Moxon and Rison, 1994; Dean, 1999). Therefore, especially mid-infrared spectroscopy is widely used to reveal the presence of water in gem and other mineral species (Farmer, 1974; Frondel, 1982; Stockton and Fritsch, 1987; Foldvari, 1991; Yamagishi et al., 1997). Meanwhile, the initial included waters in all mineral species can be divided into three groups, namely the hydroxyl (OH) group located at structural defects, surface hydroxyls hydrogen-bonded to each other (H-O-H) and free molecular water (H_2O) (Taylor et al., 1970; Dean, 1999).

In addition, the vibration range between 200 and 1100 cm^{-1} of the mid-infrared region includes the most important absorption peaks to identify opaline-quartz, chalcedonic-quartz, and crystalline-quartz structures (MSHA, 1994). Absorption due to the silica phases forming these silica structures, such as pseudocrystalline cristobalite-tridymite (opal-CT), pseudocrystalline cristobalite (opal-C) and amorphous silica (opal-A or AS) for the opaline quartz structure; cryptocrystalline quartzes (chalcedony-Ch and moganite-M) for the chalcedonic quartz structure and full crystalline alpha- or beta-quartz (Q), cristobalite (C), tridymite (T) for the crystalline quartz structure can be seen in the 700-1000 cm^{-1} region of the infrared spectrum (Farmer, 1974; Frondel, 1982; Stockton and Fritsch, 1987; Foldvari, 1991; MSHA, 1994;Yamagishi et al., 1997).

The mid-infrared spectrum of Biga chryoprase is given in Fig. 3.11. The mid-infrared spectrum of Biga chrysoprase in the range from about 200 to 4000 cm^{-1} at room temperature shows many vibrational transmission bands related to microcrystalline silica building phases, hydroxyl group water, and metal ion impurities. Accordingly Table 3.2 displays the assignments of these bands in Biga chrysoprase.

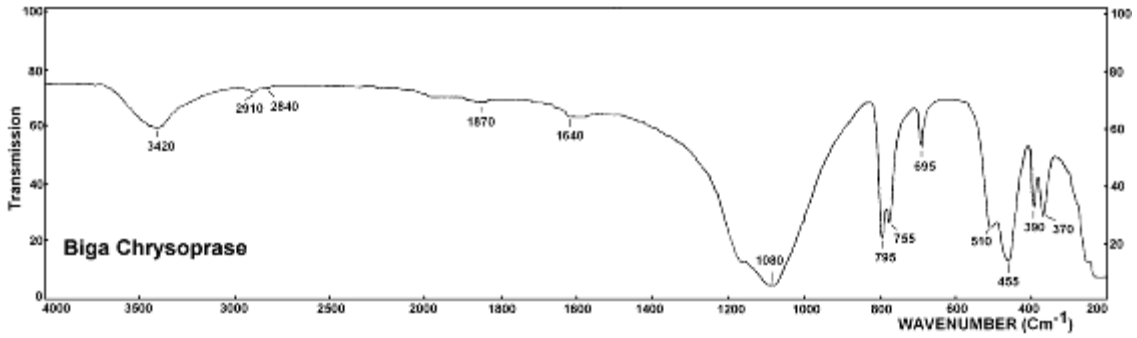

Figure 3.11 The mid-infrared transmission spectrum of the representative Biga chrysoprase, obtained at room temperature.

Table 3.2 Assignments of the infrared (IR) bands of Biga chryoprase.

ν (cm^{-1})	Assignment
3420	**"OH" stretch "H-O-H" stretch**
2910 2840	**"Si-O" vibration**
1870	**"Si-O" vibration**
1640	**"OH" bending of water "H-O-H" bending of water**
1165	**Main metallic trace element implications,"Fe, Cr, Ni"**
1080	**Asymmetric Si≡O≡Si stretching**
795 755	**Silica building phases and related inclusions**
695	**"OH" stretch**
510	**Additional vibration**
455	**Additional vibration**
390	**Additional vibration**
370	**Additional vibration**

3.6 Chemistry (XRF and ICP-AES)

The Biga chrysoprase was examined using X-ray fluorescence (XRF) and inductive coupled plasma-atomic emission spectroscopy (ICP-AES) for analyses and detections. Table 3.3 shows the average chemical contents.

Table 3.3 Average bulk and trace element chemical analyses of the representative Biga chrysoprase sample. Relatively higher concentrations of trace elements, such as Fe, Cr, Mn, As, Ni, Pb, Sb, and Zn are unique characteristics of Biga chrysoprase.

Oxides %	Instrument (XRF)	Sample	Elements	Instrument (ICP-AES)	Sample
	Detection limits	**Biga Chrysoprase**		Detection limits	**Biga Chrysoprase**
SiO_2	0.01 %	95.50			
Al_2O_3	0.01 %	0.99	Al	0.01 %	0.54
Fe_2O_3	0.01 %	1.98	Fe	0.01 %	**1.36**
CaO	0.01 %	0.06	Ca	0.01 %	0.06
MgO	0.01 %	0.12	Mg	0.01 %	0.04
Na_2O	0.01 %	0.13	Na	0.01 %	0.03
K_2O	0.01 %	0.18	K	0.01 %	0.13
Cr_2O_3	0.01 %	0.15	Cr	1 ppm	**823**
TiO_2	0.01 %	0.02	Ti	0.01 ppm	0.01
MnO	0.01 %	0.03	Mn	5 ppm	**184**
P_2O_5	0.001 %	0.013	P	10 ppm	20
SrO	0.01 %	0.01	Sr	1 ppm	17
BaO	0.01 %	0.01	Ba	10 ppm	20
LOI	0.01 %	0.64			
Total	0.01 %	**99.83**			
			Ag	0.5 ppm	2.5
			As	5 ppm	**126**
			Be	0.5 ppm	<0.5
			Bi	2 ppm	<2
			Cd	0.5 ppm	0.8
			Co	1 ppm	4
			Cu	1 ppm	13
			Ga	10 ppm	<10
			La	10 ppm	<10
			Mo	1 ppm	2
			Ni	1 ppm	**4600**
			Pb	2 ppm	**417**
			S	0.01 ppm	0.01
			Sb	5 ppm	**154**
			Sc	1 ppm	1
			Th	20 ppm	<20
			Tl	10 ppm	<10
			U	10 ppm	<10
			V	1 ppm	8
			W	10 ppm	<10
			Zn	2 ppm	**192**

The main chemical bulk concentrations of these chrysoprase materials which occur in the silicified serpentinitic host rock are as follows; SiO_2 (95.50%), Al_2O_3 (0.99%), CaO (0.06%), MgO (0.13%), Na_2O (0.12), K_2O (0.18%), and Cr_2O_3 (0.15%). In addition, some trace element concentrations are also very distinctive, such as Fe (13600 ppm), Ni (4600 ppm), Cr (823 ppm), Pb (417 ppm), Mn (184 ppm), Sb (154 ppm), Zn (192 ppm), and As (126 ppm). Some of these trace elements

can be found in any chrysoprase sample from Poland, Kazakhistan, Australia, and Tanzania (Sachanbinski et al., 2001; Skrzypek et al., 2003, 2004), even though the concentrations of some are unusual.

3.7 Dispersive (Green Laser) Confocal Micro-Raman (DCμRS) Spectroscopy

Micro-Raman spectroscopy provides a unique method for characterizing the crystal chemical properties of heterogeneous samples. The technique is now routinely used to establish the identity of an unknown gem, study inclusions, and characterization. Also, the spatial resolution and ease of data collection of this technique are particularly useful for rapid identification of minerals in thin section (Mao et al., 1987). Because of the sensitivity of vibrational frequencies and scattering intensities to slight differences in crystal structures (i.e., bond angles, site symmetries and lattice vibrations), such vibrational spectroscopic methods are also well suited for distinguishing among mineral polymorphs (Kingma and Hemley, 1994).

The dispersive (green laser) confocal micro-Raman spectrum of the representative Biga chrysoprase and green-stained Biga quartz in the range between 50 and 1600 cm^{-1} was examined to investigate the vibrational and structural characteristics of the component phases, including their spatial distribution (Figure 3.12). It is important to note that these Raman bands have not been reported in any previous references. Therefore, it was not possible to compare and contrast with the data from previous studies.

A total of 14 vibrational micro-Raman bands of Biga chrysoprase and a total of 7 vibrational micro-Raman bands of green-stained Biga quartz were established. They were firstly classified as the main vibrational bands of chalcedony, moganite, and alpha quartz in Biga chrysoprase and green-stained Biga quartz (Table 3.4), and then possible causes of those in Biga chrysoprase were inferred (Table 3.5).

Table 3.4 Micro-Raman finger-prints belonging to the main vibrational bands of chalcedony, moganite, and alpha quartz in Biga chrysoprase and green-stained Biga quartz.

Biga Chrysoprase			**Ideal Fibrous Moganite**	**Ideal Fine-Grained Alpha Quartz**	**Green-Stained Biga Quartz**
Fibrous Chalcedony	**Fibrous Moganite**	**Fine-Grained Alpha Quartz**			
υ (cm^{-1})	**υ (cm^{-1})**	**υ (cm^{-1})**	**υ (cm^{-1})**	**υ (cm^{-1})**	**υ (cm^{-1})**
126					**126**
				128	
			129		
139					
			141		
		206		206	**206**
			220		
259					
			265	265	
			317		
352					**351**
				355	
			370		
			377		
		394		394	
			398		
				401	
			423		
			449		
				450	
460					
			463		
				464	**464**
	501		501		
				511	
549					
			693		
				696	
			792		
				796	
				808	
			833		
			1058		
				1069	
1082					
			1084		
				1085	
1160					
				1162	
			1171		
			1177		
				1230	
					1293
1303					
					1408
1430					
1577					
					1579

Not: Ideal moganite and alpha-quartz Raman peak data were compiled from Kingma and Hemley (1994).

Table 3.5 Confocal micro-Raman vibrational bands of the representative Biga chrysoprase, and their inferred causes according to symmetry and Raman activity of SiO_4 tetrahedron with Td symmetry (the inferences were modified from Kingma and Hemley, 1994; Colomban and Prinsloo, 2009).

Peak Number	Micro-Raman Bands Wavenumbers / cm^{-1}	Inferred Causes
1	**1577**	Single nonbridging oxygen hole centres with several precursors (i.e., hydroxyl group, peroxy linkage) and oxygen vacancy.
2	**1430**	Doubly nonbridging oxygen hole centres with several precursors (i.e., hydroxyl group, peroxy linkage) and oxygen vacancy.
3	**1303**	
4	**1160**	ν_1 doubly asymmetric stretching modes of degeneracy of [SiO_4/M] centres. The "M" includes the some cationic substitutions of Si by Fe, Cr, Mn, As, Ni, Pb, Sb, and Zn, and also K and Na.
5	**1082**	
6	**549**	ν_1 single symmetric stretching modes of degeneracy of [SiO_4/M] centres. The "M" includes the some cationic substitutions of Si by Fe, Cr, Mn, As, Ni, Pb, Sb, and Zn, and also K and Na.
7	**501**	ν_2 doubly symmetric bending mode of $[SiO_4]^{4-}$ tetrahedra of moganite (length-slow chalcedony) inclusion.
8	**460**	ν_2 doubly symmetric bending mode of of $[SiO_4]^{4-}$ tetrahedra.
9	**394**	ν_4 doubly symmetric bending modes of degeneracy of [SiO_4/M] centres. The "M" includes the some cationic substitutions of Si by Fe, Cr, Mn, As, Ni, Pb, Sb, and Zn, and also K and Na.
10	**352**	
11	**259**	Single rotational libration mode.
12	**206**	Single translational libration mode.
13	**139**	Doubly translational libration modes.
14	**126**	

As seen in the Tables, the most distinctive and strong micro-Raman peaks in Biga chryoprase are due to the microcrystalline chalcedonic quartz phase (fibrous length-fast chalcedony) as a main peak at 460 cm^{-1}. The region at 1000-1600 cm^{-1} of the chrysoprase spectrum is characterized by broad features resembling the spectral characteristics of a microcrystalline material in this region. The spectrum shares common features that can be correlated to similar motions of Si and O atoms within the framework structures of the tetrahedrally coordinated silica phases (McMillan and Hess, 1990; Kingma and Hemley, 1994; Colomban and Prinsloo, 2009).

The other important micro-Raman peak is due to the microcrystalline interval quartz phase (fibrous length-slow moganite) inclusion. The strong band of the interval moganite phase, which is a structurally distinct polymorph of silica assuming the monoclinic structure, was found at 501 cm^{-1} for Biga chrysoprase. Similarly,

some investigations previously reported for moganite in microcrystalline silica samples have suggested that this strong band was found at 501 cm^{-1} (Kingma and Hemley, 1994). A supplementary Raman band at 501 cm^{-1} in microcrystalline samples has often been used for the evaluation of the quartz/moganite ratio. In addition, it may be stated that the 501 cm^{-1} Raman band is due to 'free' Si-O vibrations of non-bridging Si-OH that oscillate with a higher natural frequency than bridging Si-O-Si.

On the other hand, the spectra in Figures 3.13 and 3.14 show a combination of the mapped Raman spectra and related microscope images (Figure 3.13), and also the overlapped and separated Raman spectra which were compared with that of the ideal microcrystalline chalcedonic quartz phase (fibrous length-fast chalcedony) in the library of device (Figure 3.14).

The most recent technological developments in Raman spectroscopy have enabled rapid mapping (Gouadec and Colomban, 2007; Colomban and Prinsloo, 2009; Carter et al., 2010). Rapid mapping capabilities allow the large scale survey maps to be collected first and smaller, higher spatial resolution maps obtained once a region of interest has been located. The large scale map and the related microscope images of the Biga chrysoprase suggest the existence of the same bands (Figure 3.13).

Finally, the bands obtained in the spectrum of the Biga chrysoprase were matched with the bands in the spectrum of ideal chalcedony both in the spectrometer library and in the well-known database (RRUFF, 2012). Comparison and contrast of these Raman bands show that the bands of the Biga chrysoprase are highly similar to those of ideal chalcedony, which form the microcrystalline chalcedonic-quartz texture (Figure 3.14).

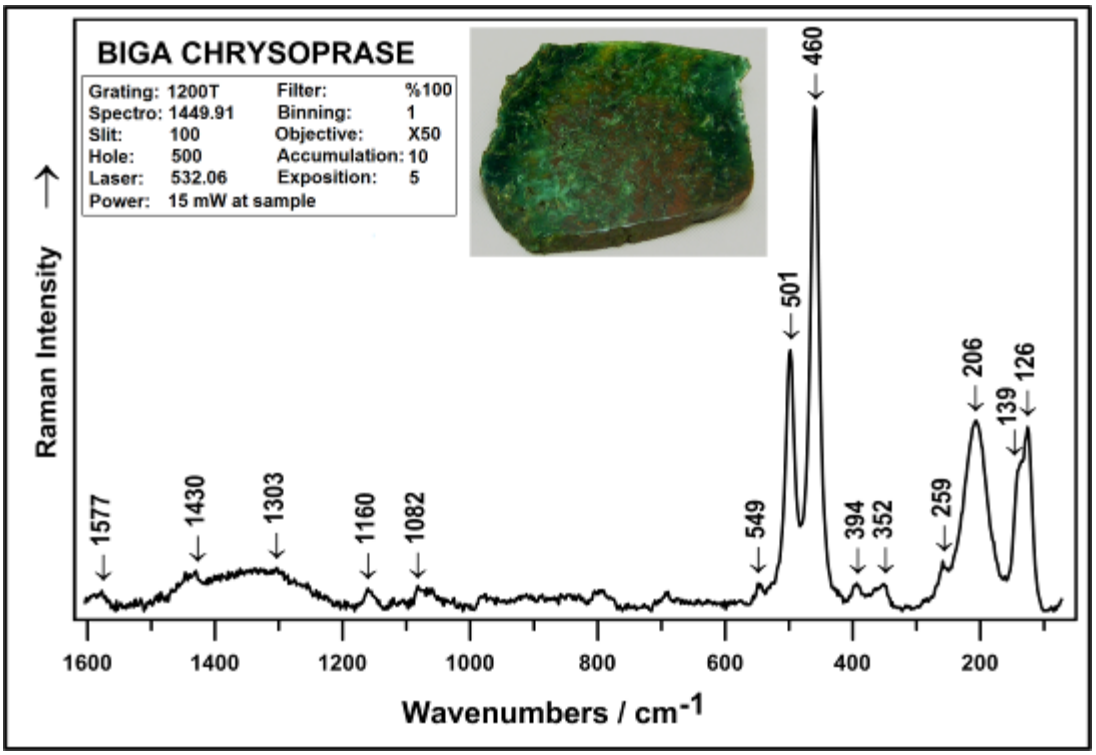

Figure 3.12 The dispersive (green laser) confocal micro-Raman vibrational bands in the Biga chrysoprase spectrum representing the microcrystalline chalcedonic quartz phase (fibrous length-fast chalcedony) as a main peak at 460 cm^{-1}, and the inclusion microcrystalline interval silica phase (fibrous length-slow moganite) as a main peak at 501 cm^{-1}.

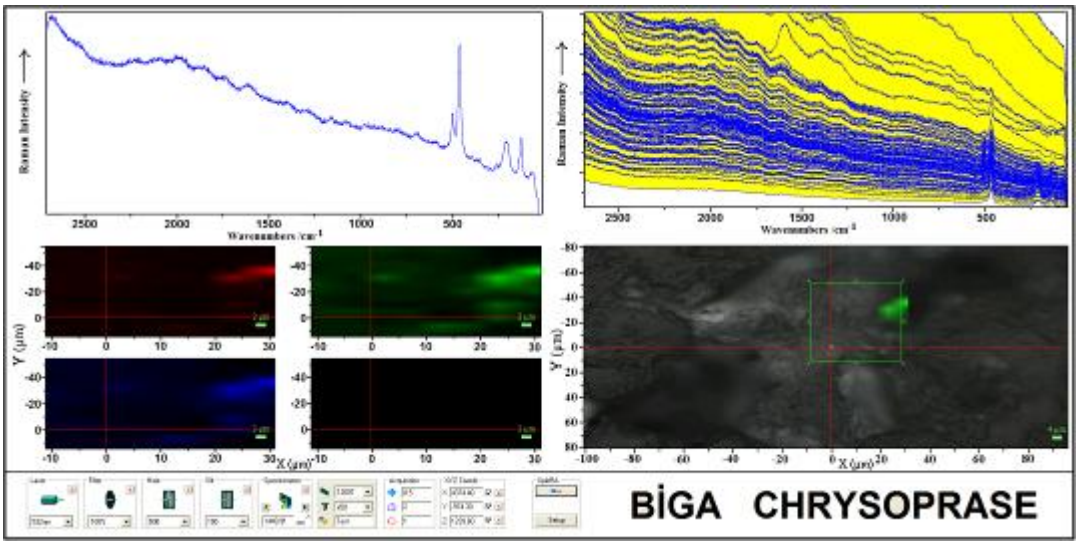

Figure 3.13 The mapped multi spectra and related microscope image of Figure 3.12. They show the variation of any fitted parameter (i.e. intensity, width or position of one band) as a function of the point of analysis. If the mapping is regular and sufficiently tight, one gets a ‘‘smart map’’ of the parameter (color or contrast scaling) superimposed with the optical image of the probed area.

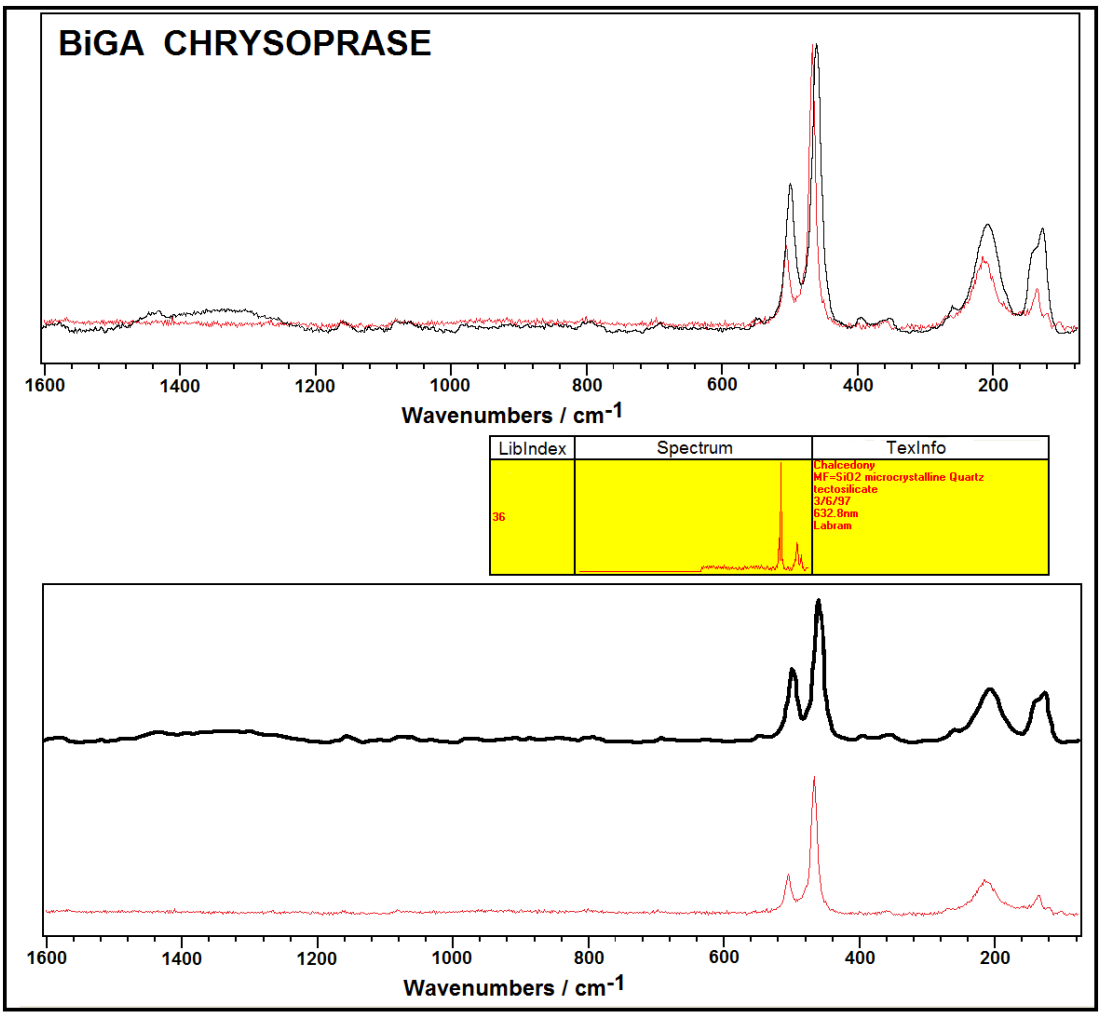

Figure 3.14 A comparison of the micro-Raman bands of fibrous chalcedony in Biga chrysoprase with those of the ideal fibrous chalcedony in the library of the device.

On the other hand, in the same deposit, massive green-stained quartz masses are also present, and they are common and have a low-quality in terms of gemmological importance. Thus, it is necessary to distinguish these masses from each other non-destructively. Dispersive confocal micro-Raman spectroscopy (DCμRS) help to clearly distinguish the chalcedonic-quartz silica building phase (fibrous chalcedony) from the crystalline-quartz silica building phase (fine-grained alpha-quartz) in both chrysoprase and green-stained quartz masses in this deposit. The representative Raman spectrum of the massive green-stained quartz mass is given in Figure 3.15, and the overlapped and separated Raman spectra which were compared with that of ideal quartz are given in Figure 3.16. Ultimately, in order to compare these two

Raman spectra, the combined Raman spectra showing the chalcedonic-quartz silica phase and the crystalline-quartz silica phase are given in Figure 3.17.

Because alpha-quartz, chalcedony and moganite share many of the same structural elements, it is not surprising that the chalcedony vibrational spectrum most closely resembles that of alpha quartz. Despite the similarity in the character of the fibrous chalcedony and fine-grained alpha quartz vibrational spectra, there exists a significant variation in the positions of the similarly shaped peaks for the two important silica building phases.

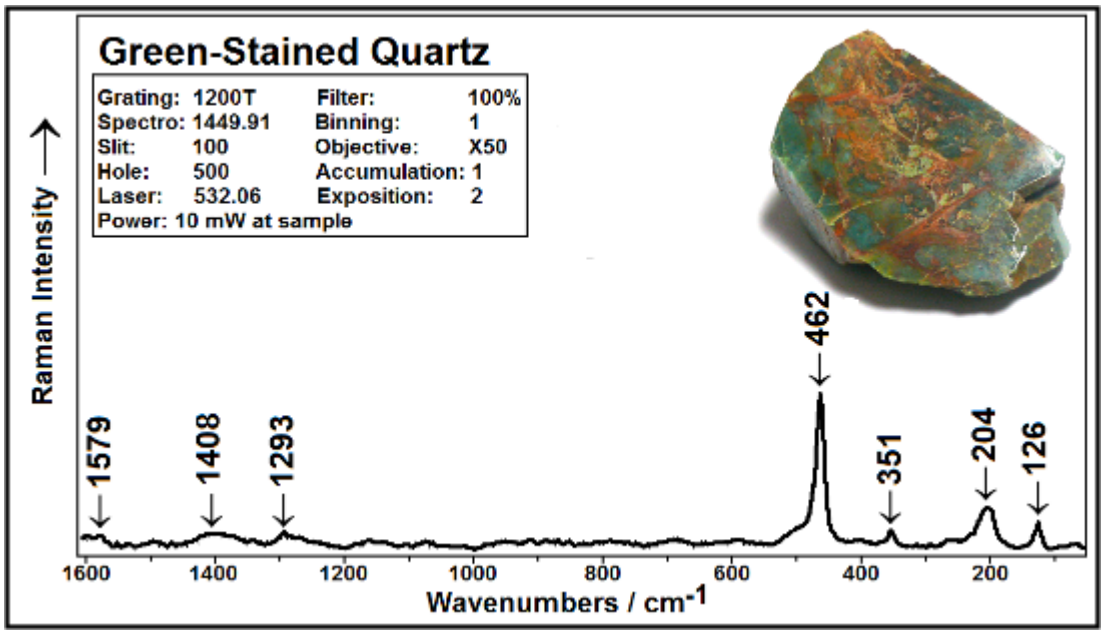

Figure 3.15 The dispersive confocal micro-Raman vibrational bands in the spectrum of the green-stained Biga quartz, found in the same deposit. It is common and low-quality in terms of gemmological importance.

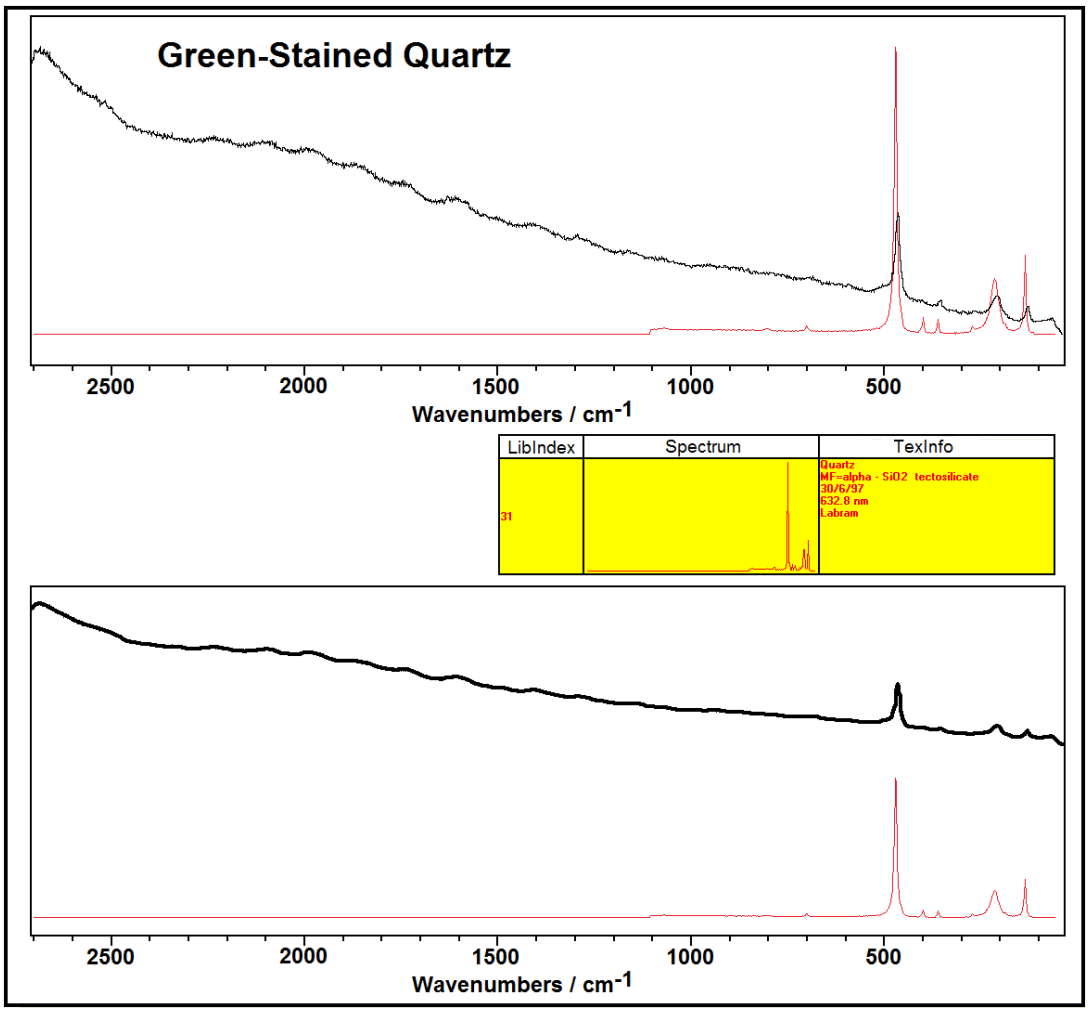

Figure 3.16 A comparison of the micro-Raman bands in the green-stained Biga quartz with that of the ideal fine-grained alpha-quartz in the library of the device.

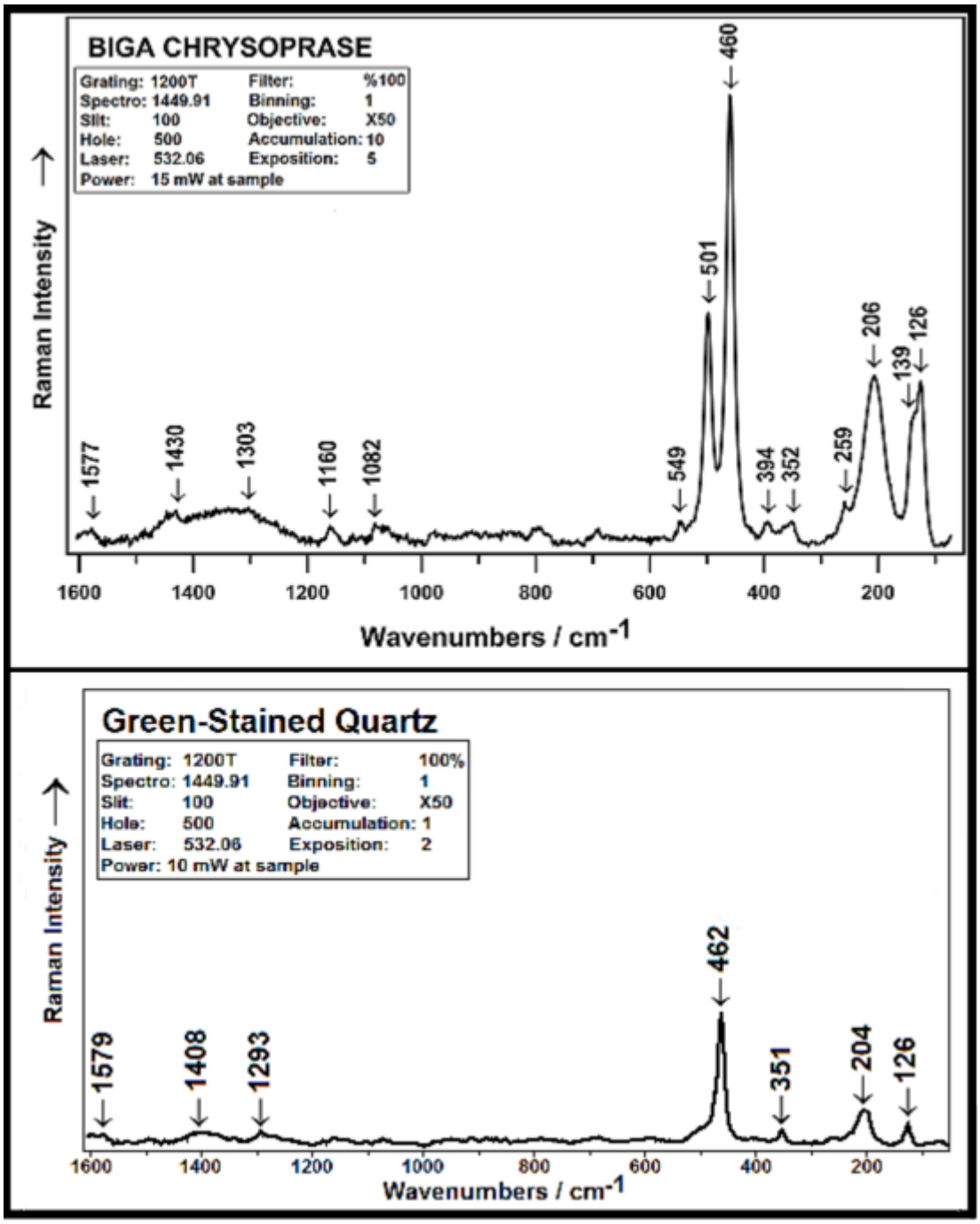

Figure 3.17 Combined Raman spectra of the chalcedonic-quartz and crystalline-quartz, seen in Figures 3.12 and 3.15.

All collective vibrations in the crystals can be viewed as the superposition of plane waves that virtually propagate to infinity. These plane waves (the normal modes of vibration) are commonly modeled by quasi-particles called photons. A normal coordinate of the form $Q=Q_o\cos(2\pi\nu n_{vib}t)$, which is actually a linear combination of bond lengths and bond angles, is associated with each normal mode. Depending on the dominant term in the normal coordinate, these modes can be classified as either stretching (n), bending (d), torsional (t), librational (R0/T0 pseudorotations/translations) or lattice modes (the latter include the relative displacement of the unit cells) (Vandenabeele, 2010; Slodczyk and Colomban, 2010; Gouadec and Colomban, 2007; Colomban and Prinsloo, 2009).

The production of the Raman bands of the Biga chrysoprases can be attributed mainly to extrinsic defects (chemical impurities), which are due to increasing amounts of tetrahedral character with increasing electron density caused by the presence of trace elements, taking into consideration the increased ionic character of the Si–O and Al–O bonds in the alkali silicate (Weil, 1984), and partially to intrinsic defects (the nonbridging oxygen deficient centers with several precursors and self-trapped excitation). While the ionic bond character is dominant for Si-O bonds, covalent bond contributions become more significant and the basicity increases when the Si-O-Si angle is reduced from linearity to values near the tetrahedral angle. Thus, the existence of the exceptional intermolecular hydrogen bond can be explained by its very small strained Si-O-Si angle that adopts nearly a tetrahedral angle.

Nutall and Weil (1980) reported a hydrogenic trapped holecenter with four hydrogen atoms in a regular silicon lattice position. Since, in the case of some elements, a compensation of the electric charge is necessary, additional cations such as H, Li, Na., K, and Ag can be incorporated in inter-lattice positions in conjunction with structural channels. The nonbridging oxygen hole center (≡Si–O) is described as a hole trapped in a single oxygen atom bound to a single silicon on three oxygen atoms in the SiO_2 structure (Weil, 1984). Oxygen excess centers include the peroxy radical (≡Si–O–O), the hole centers consisting of an O^{2-} ion bonded to single silicon on three oxygen atoms, and the peroxy linkage (≡Si–O–O≡). A further type of defect

is OH^- centers which consist of a proton bound on a regular lattice O^{2-} ion, located between two O^{2-} ions of the SiO_4 tetrahedron. Because of the negative net charge, additional trivalent substitutes of the Si^{4+} positions occur as the charge compensation (i.e. Al^{3+}) in such a way that an additional proton is bound on the Al^{3+} (Vandenabeele, 2010; Gouadec and Colomban, 2007; Colomban and Prinsloo, 2009).

However, the contribution of ionic bonds like Al-O is null according to that of covalent Si-O bonds (Colomban and Prinsloo, 2009). So, the considerable strength of the Si–O bond results in a high melting temperature (Colomban and Prinsloo, 2009). The basic unit of a silicate, the SiO_4 tetrahedron, is a strong chemical entity and the possibility to share oxygen atoms between two tetrahedra with variable Si–O–Si angles or to have non-bridging oxygen atoms gives a polymeric character to silicates (Colomban and Prinsloo, 2009). The $[SiO_4]^-$ center is caused by substitution for Si^{4+} with an electron hole at one of the four nearest O^{2-} ions, forming O^-.

Slodczyk and Colomban (2010) have stated that many electrical/electrochemical/magnetic properties result from a competition between different potentials of the chemical bonding and structure. In general, some atoms (alkali and earth alkali cations) have a strong ionic character. Some other atoms develop covalent bonding (i.e., transition metals) and form strong ‘‘molecular’’ bricks. Metallic bonds can also be formed between atoms such as Ag, Cu, Tl, and ionized clusters intermediately between ions and complex nano-clusters may be observed (Slodczyk and Colomban, 2010).

Gouadec and Colomban (2007) have stated that the width of the other Raman modes is mainly sensitive to the ‘‘local’’ crystal field; more specifically to the short range order in the first (0.1–0.5 nm) and second (0.5–5 nm) atomic shells. If the ‘‘molecular’’ description of vibrations applies, then Raman bending modes are even specifically sensitive to local geometric disorientation and Raman stretching modes to the neighboring disorder (particularly atoms from other sub-lattices or electric defects resulting from substitutions / vacancies) (Gouadec and Colomban, 2007).

3.8 Color Origin of Biga Chrysoprase

The optical absorption spectroscopy (OAS) indicates that the dark green coloration of the Biga chrysoprase is due to light transmittance at 528 nm as a result of absorbance peaks at 645 and a 360-410 nm absorbance band gap (Figure 3.18). These aborbances may be related to the major proportions of certain impurity ions. However, ICP-AES analysis suggests that the color agencies in Biga chrysoprase are not only Ni ion content (4600 ppm) but also Fe ion (13600 ppm) and Cr ion (823 ppm) contents. In addition, shifts or broadenings of this absorbance peak and band gap produce color hues between dark and light green in the chrysoprase.

The green color of chrysoprase is known to originate from a compound containing nickel incorporated in the microcrystalline chalcedony matrix. The nature of the admixed nickel containing phase is not known precisely due to the lack of direct evidence from microscopy or X-ray diffraction. Rossman (1994) has stated that optical spectra indicate Ni^{2+} in octahedral co-ordination, and he has indicated that bunsenite (NiO) has been suggested as a coloring agent. Therefore, the color of chrysoprase, in general, is due to the nickel incorporated in the quartz.

The mainly dark green coloration of the Biga chrysoprases is due to a complex mechanism, since many transition metals, which are coloration agents, are present. Some of the elements Fe, Cr, and Ni (Table 3.3) are certainly responsible for the coloration as external lattice defects. However, nickel is the main ion responsible for producing the dark green color (Nagase et al., 1997; Sachanbinski et al., 2001; Witkowski and Zabinski, 2004; Befi, 2009; Shigley et al., 2009; Graetsch, 2011). Some trace elements, such as iron and chromium ions modify the typical green color of the chrysoprases by adding a brownish hue, but in order to clarify this colororation mechanism, further investigations will be necessary. Although Nagase et al. (1997) and Sachanbiński et al. (2001) identified with electron microscopy nanometre size inclusions of Ni-bearing phyllosilicates of low crystallinity in chrysoprase from Australia, Poland and Kazakhstan, Graetsch (2011) describes evidence of the presence of the nickel carbonate mineral gaspeite in chrysoprase from Tanzania.

Nagase and his colleagues (1997) tried to identify the origin of the green color in the chrysoprases from Warrawanda, Western Australia. Their TEM observations and IR-spectra analyses show that the chrysoprases include kerolite, which occurs as a cotton-like aggregate of extremely fine-grained crystals at the boundaries of coarse grains in the quartz crystals. Their EPMA analyses show that the kerolite contains about 10 wt% NiO, and that NiO content of the chrysoprase increases with the degree of silicification of the surrounding serpentinite. The Ni-bearing kerolite derived from the silicified serpentinite is inferred to production of the typical green color of the chrysoprases (Nagase et al., 1997).

In a recent study, Graetsch (2011) revealed that the green colour of the chrysoprase from Haneti (Tanzania) is caused by the incorporation of 0.47(6) wt. % gaspeite (a Ni-carbonate mineral) in the microstructure of microcrystalline quartz in contrast to the chrysoprases from other localities. Additionally, chrysoprase samples from the comparison sources (Poland and Australia) did not show any gaspeite diffraction peaks; their color seems to originate from a different pigment (i.e., inclusions of poor crystallinity). The Haneti chrysoprase has a higher crystallinity of both the microcrystalline quartz matrix and the gaspeite pigment (Graetsch, 2011).

In addition, Heflik et al. (1989) studied chrysoprase found in altered serpentinites that occur within a nickel deposit in lower Silesia. The authors were able to determine that the color was caused by tin and suggested the tin may by incorporated in the mineral as a distinct phase in bunsenite (NiO).

Ultimately, it can be stated that some of the trace elements found in this study (mainly nickel) are certainly responsible for the production of both the characteristic green color and the Raman vibrational bands.

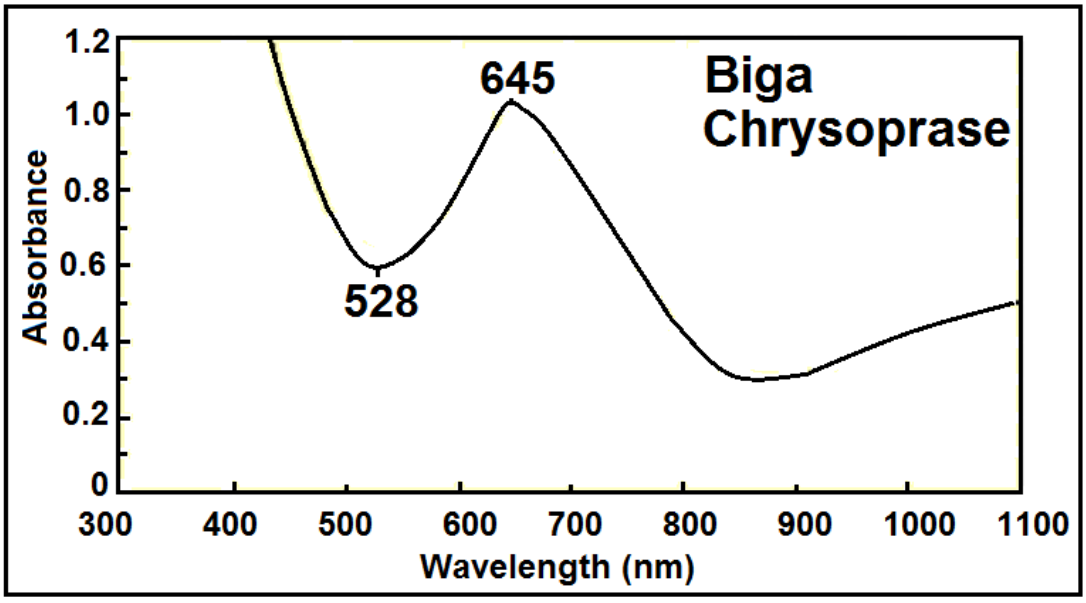

Figure 3.18 The optical absorption spectrum comprising UV-Vis-NIR regions. Light transmittance at 528 nm in the visible region as a result of absorbance peaks at 645 and a 360-410 nm band gap produces the dark green coloration of Biga chrysoprase.

3.9 Luminescence (PL, CL, TL)

It is well-known that some luminescences are the emission of light from a material when excited by

- UV (photoluminescence, PL)
- Electrons (cathodoluminescence, CL)
- Heat (thermoluminescence, TL).

Indeed, perfect-structured crystalline materials emit very little light when excited by irradiation and/or heating. Therefore, all kinds of luminescence of minerals (and materials) tell us about the crystalline defects that occur in all natural solids. These are (1) chemical impurities, such as trace elements, (2) structural imperfections, such as vacancies (holes where atoms should be), elements with the wrong charge (O^{1-} where O^{2-} should be), dislocations (where bonds do not join up properly), and (3) many others (Blasse and Grabmaier, 1994; Gaft, 2005; Handerson and Imbusch, 2006). Different luminescence centres produced by cathodoluminescence (CL), radioluminescence (RL), and photoluminescence (PL), and excitation using

irradiation, are due to the overall signals, even though thermoluminescence (TL) sensitivity varies depending on the treatment of the chrysoprase samples.

During this investigation, three different luminescence spectra of the Biga chrysoprase samples [photoluminescence-PL (Figure 3.19), cathodoluminescence-CL (Figures 3.20-3.22), and thermoluminescence-TL (Figure 3.23)] were taken into consideration, and evaluated.

3.9.1 Photoluminescence (PL)

Photoluminescence (PL) excitation emission scans of Biga chrysoprase were obtained for the first time in three dimensions (3-D) to characterize a variety of the material parameters, and spectral-colored photoluminescence (PL-3D) morphologies and (PL-2D) graphics are given in Figure 3.19. These spectral characteristics ranging between wavelengths of 300 and 900 nm, and temperatures between 220 and 340 K, are unique to the Biga chrysoprase.

Accordingly, a total of 4 maxima peaks in the visible and near-infrared regions at a temperature of 250 K appear at 398, 413, 427, and 740 nm, respectively. As seen, three major bands are very distinctive on the spectrum and their peaks at 398, 413, and 427 are very close, almost overlapped. These bands appear at low temperature and in the purple-blue region only.

The second relatively wider band covers the near infrared region, and its maxima peak is seen at 740 nm. In addition, between these two bands, there are numerous unimportant bands in terms of sensity and magnitude.

It is a very important result that all major and minor photoluminescence bands decrease gradually towards a temperature of 290 K, and all photoluminescence bands undulate at a temperature of about 300 K.

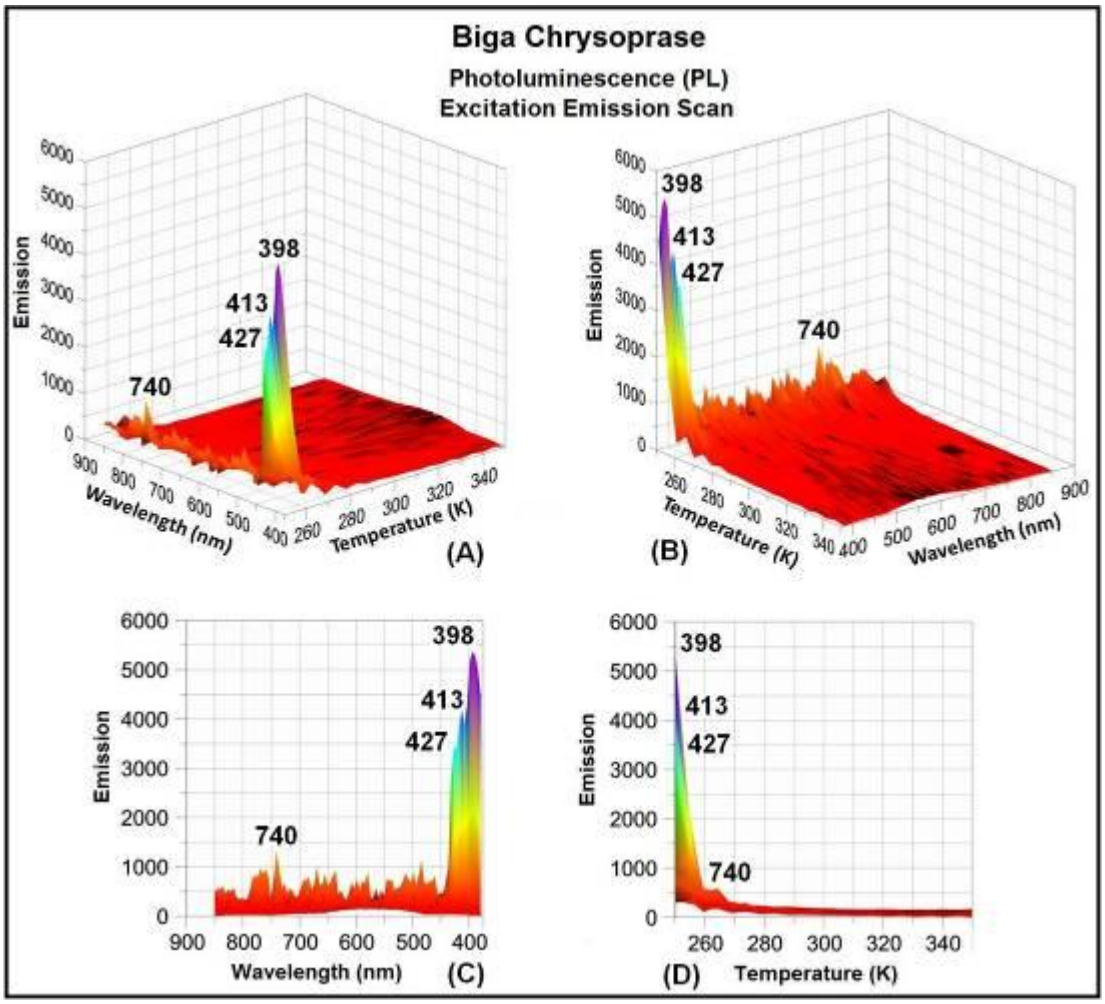

Figure 3.19 Spectral-colored photoluminescence (PL-3D) morphologies and (PL-2D) graphics of Biga chrysoprase; from the right-viewed front perspective (PL-3D) **(A)**, the left-viewed back perspective (PL-3D) **(B)**, the emission versus wavelength graphic (PL-2D) **(C)**, the emission versus temperature graphic (PL-2D)**(D)**. Major maxima peaks in the visible and near-infrared regions are measured about at 398, 413, 427, and 740 nm respectively.

In fact, what cause photoluminescence (PL) as well as other luminescence are lattice defects as either chemical impurities or structural imperfections (Blasse and Grabmaier, 1994; Gfroerer, 2000; Gaft et al., 2005; Handerson and Imbusch, 2006). Therefore, individual PL bands appearing at the end of the excitation emission scans at the negative temperature values (mainly 250 K) can be attributed to defects related to some trace element contents. Thus, it can be claimed that the majority of these defects come from cationic substations, since, PL spectroscopy provides electrical

(as opposed to mechanical) characterization, and it is a selective and extremely sensitive probe of discrete electronic states (Gfroerer, 2000).

On the other hand, in the case of obtaining information on the quality of surfaces and interfaces in Biga chrysoprase, it was revealed that the intensity and magnitude of the PL signals readable increase with Fe, Cr, Mn implications which have relatively large cationic radii. Accordingly, this situation at low temperatures can show an electrical charge changing reaction in the silica tetrahedral structure with developing strained Al(Si)-O-Fe, Al(Si)–O–Ni, Al(Si)–O–Cr, Al(Si)–O–Mn, Al(Si)–O–Pb, Al(Si)–O–Sb, Al(Si)–O–Zn and Al(Si)–O–As bonds.

3.9.2 Cathodoluminescence (CL)

Cathodoluminescence (CL-2D) spectra at room temperature produced by AC at the energies of 14 and 24 keV and DC at 24 keV display individual luminescence patterns in the investigated Biga chrysoprase samples.

The cathodoluminescence AC experimental data at 14 keV energy show that one major spectral emission band appears at readable intensity and magnitude at 90 Hz in the yellow wavelength region at 585 nm (Figure 3.20). However, both AC and DC cathodoluminescence experimental data at 24 keV show that one major spectral emission band appears, being similar to that of 14keV in readable intensity and magnitude at 90 Hz, but dissimilar to that of 14keV in the green wavelength region at 530 nm (Figures 3.21 and 3.22 respectively). In addition, because the intensities of the spectral CL emission bands at the other frequencies are very low, they can be discarded.

Accordingly, a relationship can be observed between the CL emissions and presence of some transition metal elements. Formation of the CL bands can be observed when different excitation modulation frequencies are used. However, it is obvious that all trace elements do not play a direct role.

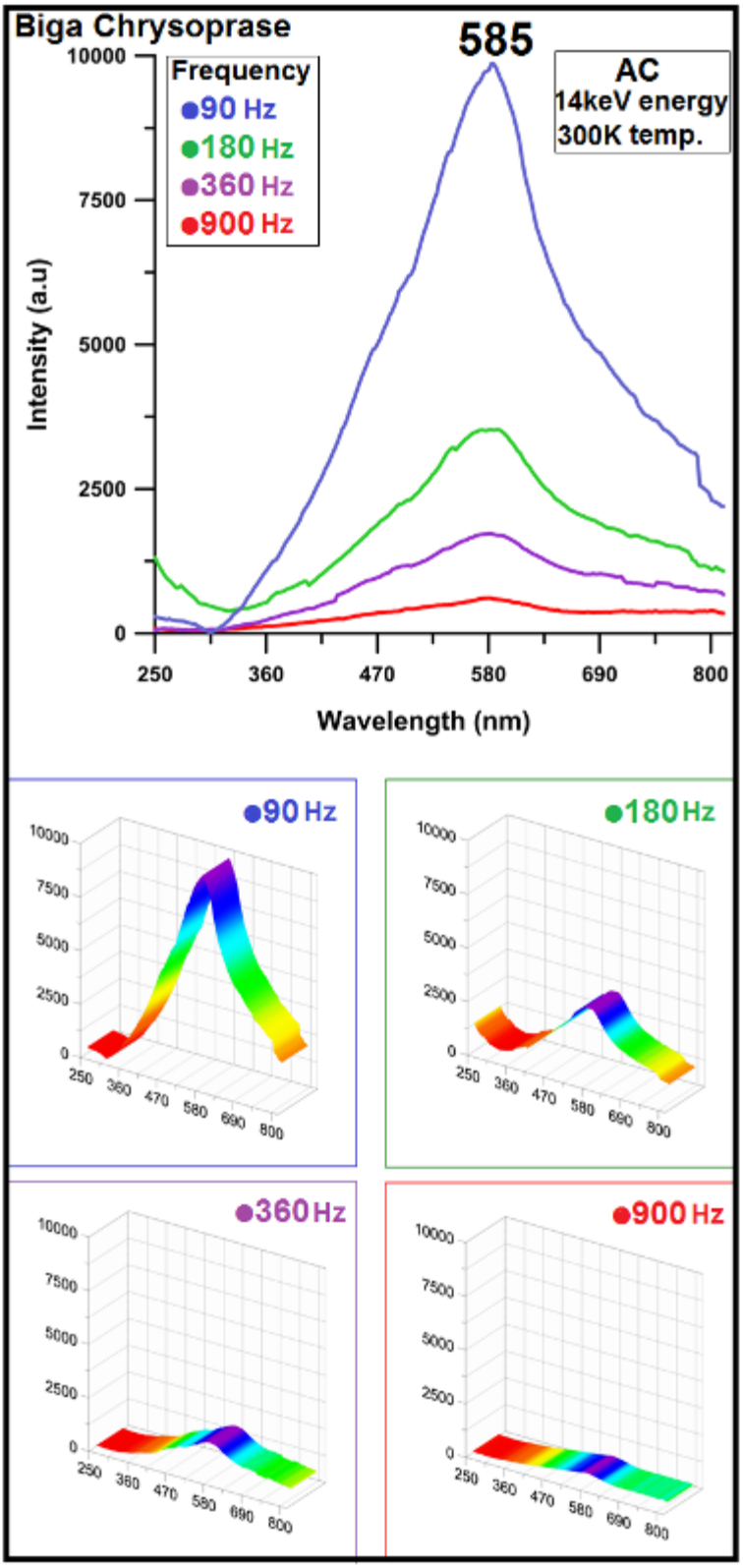

Figure 3.20 AC cathodoluminescence (CL) spectra at 14 keV energy and 300 K temperature of Biga chrysoprase. One major spectral emission band appears in readable intensity and magnitude at 90 Hz in the middle-visible wavelength region (yellow region) at about 585 nm.

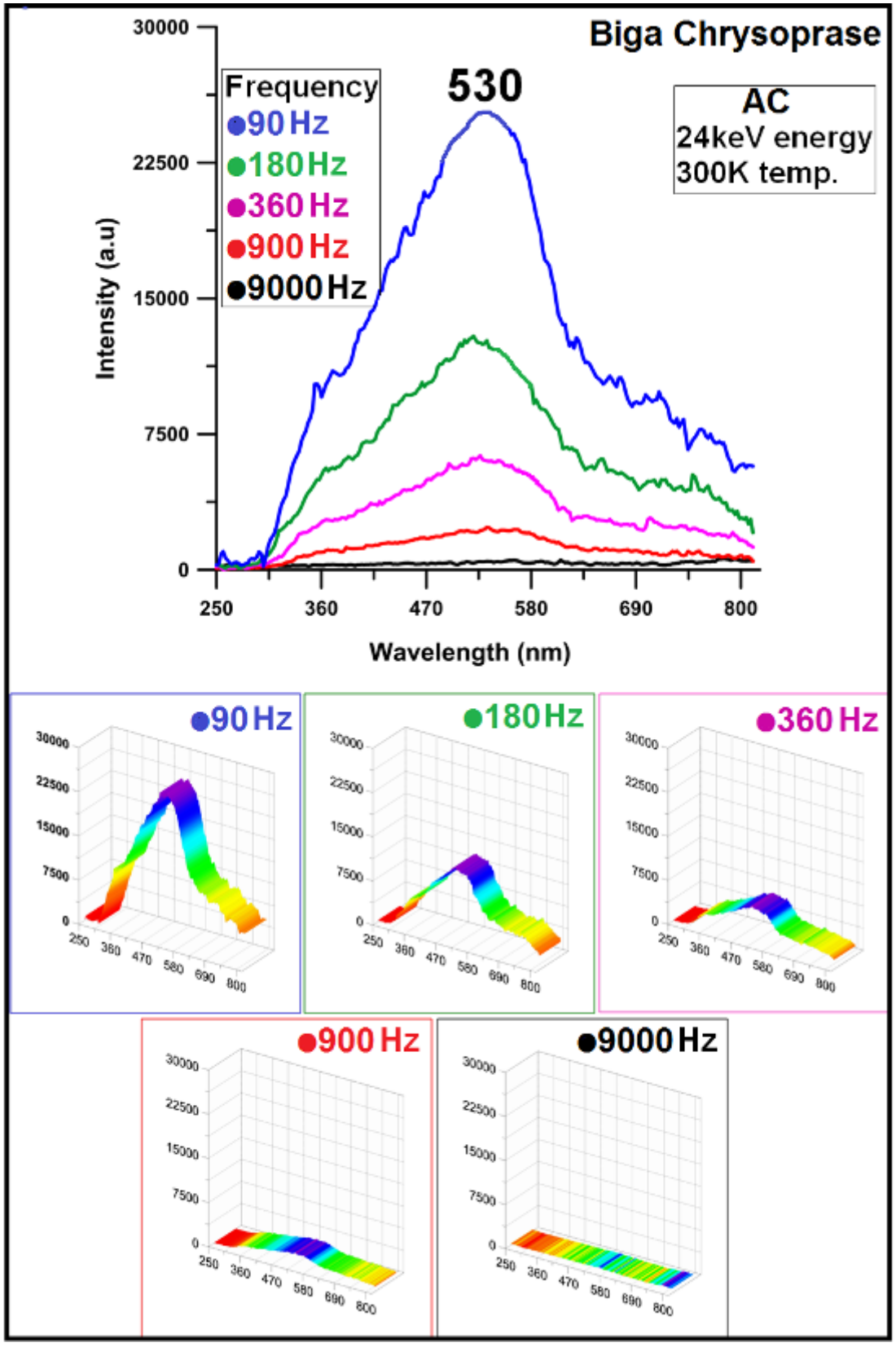

Figure 3.21 AC cathodoluminescence (CL) spectra at 24 keV energy and 300 K temperature of Biga chrysoprase. One major spectral emission band appears in readable intensity and magnitude at 90 Hz in the visible wavelength region (green region) at about 530 nm.

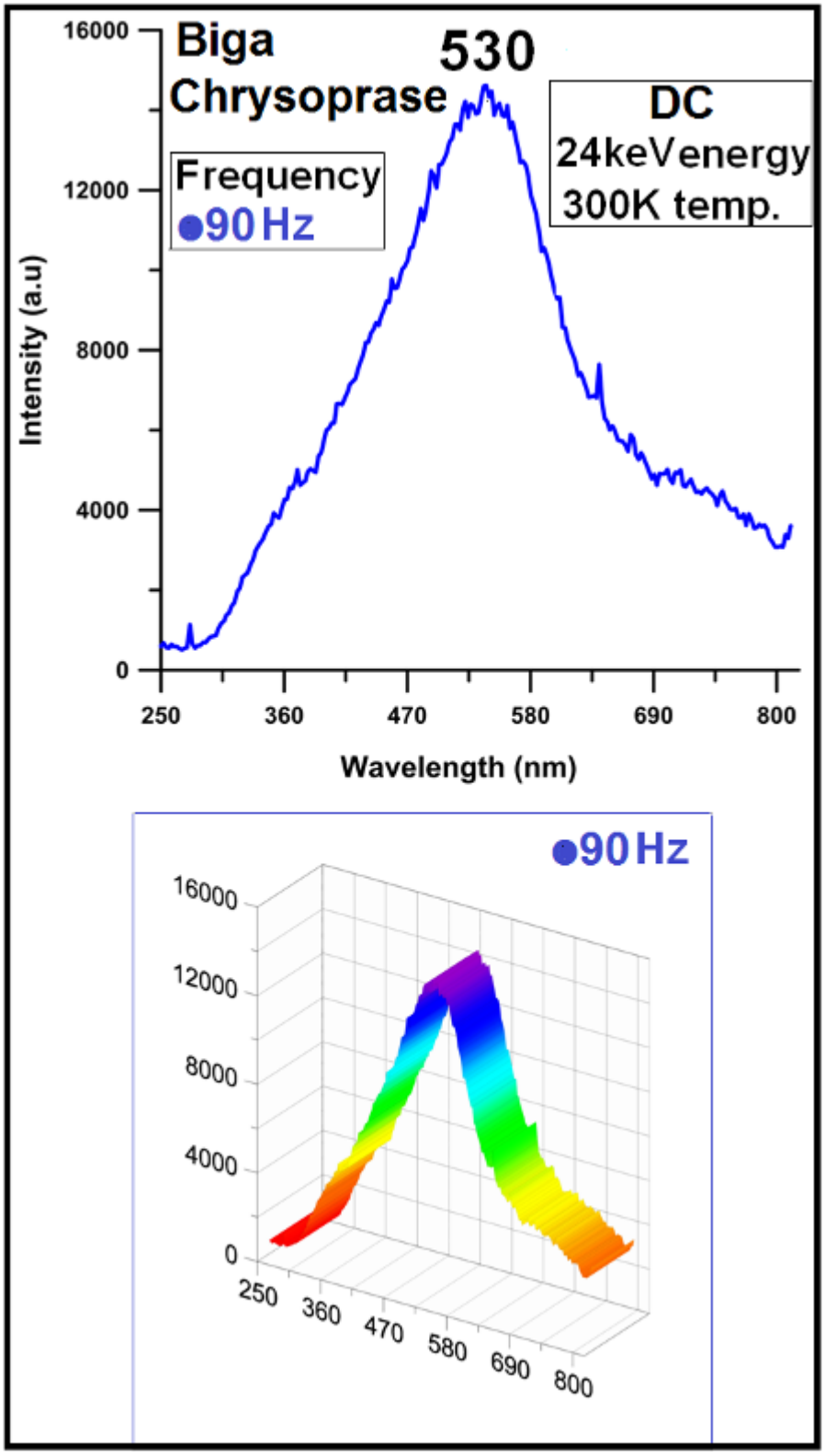

Figure 3.22 DC cathodoluminescence (CL) spectra at 24 keV energy and 300 K temperature of Biga chrysoprase. One major spectral emission band appears in readable intensity and magnitude at 90 Hz in the visible wavelength region (green region) at about 530 nm.

It can be seen that the peaks at all frequencies decrease sharply as the excitation modulation frequency increases. The fact that such changes are apparent at the very low frequencies of modulation immediately indicates that there are some very long lifetime processes occurring. This situation at room temperature can show a mechanical changing reaction in the silica structure. When the CL luminescence activators of Biga chrysoprase are considered, it is obvious that the peak-wavelengths and intensities of CL are highly dependent on the spatially varying concentrations of K, Na and Mg rather than other metal trace impurities.

As a result, it can be suggested that the remarkable CL luminescence emission in the green wavelength region (at 530 nm) in Biga chrysoprase is probably due to the silicon-oxygen and aluminium-oxygen stresses in the [SiO_4] tetrahedrons including Na, K, and Ca ions. These strained structures with Si–O bonds stabilise some non-bridging oxygen or silicon vacancy hole centres or some of the Si–O bonding defects which seem to be ultimately responsible for this kind of electron excitation.

3.9.3 Thermoluminescence (TL)

The thermoluminescence glow curve obtained as a result of a linear heating rate of 2 Cs^{-1} in N_2 atmosphere to 300 K at the end of 30 minutes has great importance for characterizing the extent of the utility of Biga chrysoprase to be used in measuring radiation doses (Figure 3.23).

Accordingly, one band peaked at 315 ^{o}C can be seen on the TL glow curve pattern. This relatively higher temperature band can be attributed to the formation conditions of the contact metamorphic zone in the Biga (Çanakkale) region. In this regard, it can be claimed that the thermoluminescence glow curve of Biga chrysoprase is one of its characteristic provenance identification methods.

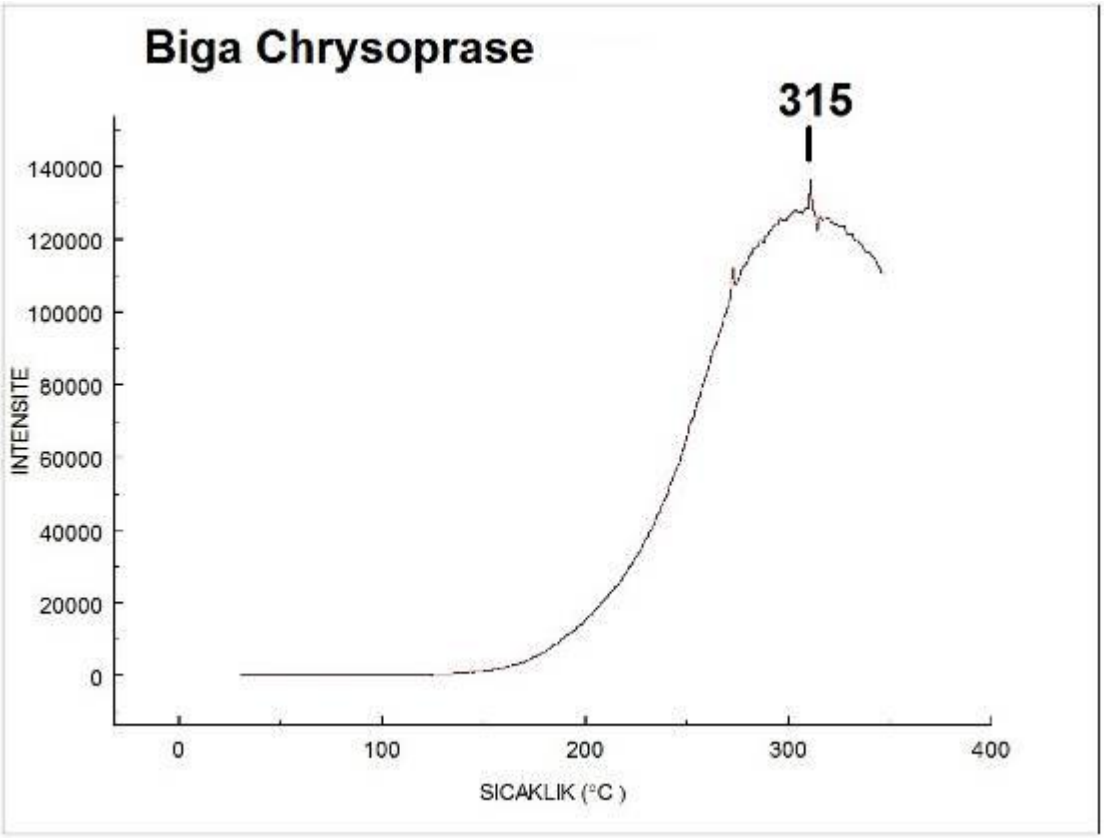

Figure 3.23 Thermoluminescence (TL) glow curve of Biga chrysoprase. On the pattern, the widest and highest band appears peaked at 315 ^{o}C.

CHAPTER FOUR
CONCLUSIONS

After the green-colored gemstone mineral deposit in the Biga (Çanakkkale) region was geologically surveyed in coarse detail, the chrysoprase samples obtained from this deposit were investigated to characterize and identify then in detail using non-destructive dispersive (green laser) confocal micro-Raman spectroscopy (DCμRS) in addition to some well-known destructive analytical methods, such as polarizing microscope, X-ray diffraction, infrared and chemical analyses, optical absorption and various luminescences. Therefore, the mineralogical differences between the real chrysoprase matrix and the green-stained quartz matrix were demonstrated.

It is well-known that the major chrysoprase producers in the last 30 years have been Poland, Kazakhstan, Australia, Brazil, and Tanzania. However, this study announces that Turkey is the newest chrysoprase producer in the world.

Conventional matrix investigation methods (polarizing microscopy, X-ray diffraction and X-ray fluorescence spectroscopies) of minerals are destructive and/or invasive, and thus, they are not used for the identification of actual silica mineral objects and/or ancient silica artifects. On the contrary, the non-destructive and/or non-invasive advantage of micro-Raman spectroscopy makes it applicable these kinds of gem materials, especially in distinguishing the alpha-quartz phase from the moganite, chalcedony, opal-CT, and opal-C phases. In addition, this method can be reliably used to distinguish all kinds of microcrystalline chalcedonic-quartz varieties (i.e. chrysoprase, blue chalcedony, agate, etc.) from all kinds of crystalline quartz varieties (i.e. rock crystal, citrine, smoky quartz, amethyst, etc.). It can be seen that DCμRS can be reliably used to identify the silica mineral species regarding their main silica building phases. Single and mapped confocal micro-Raman spectra were compared and contrasted with those of ideal micro-Raman bands in fibrous chalcedony and fine-grained alpha-quartz spectra. Rapid mapping capabilities allow large scale survey maps to be collected with smaller higher spatial resolution maps obtained once a region(s) of interest has been located. This technology was used to

investigate Biga chrysoprase. Conventional polarizing microscopic examination revealed that the chrysoprases consist of fibrous silica matrixes and centrally located inclusions of crystalline silica. The identification of these silica phases was also confirmed by X-ray powder diffraction using the comparative matching technique. However, opalline-quartz (opal-CT and opal-C) silica building phases do not exist in the Biga chrysoprase samples. Because of the existence of the chalcedonic-quartz silica interval phase (moganite) instead of the opalline-quartz silica base phase (opal-CT and opal-C), it can be stated that Biga chrysoprase from Turkey occurs at relatively higher formation temperature conditions, and this structural feature distinguishes Biga chrysoprase from the other chrysoprases from Poland, Kazakhstan, Australia, Brazil, and Tanzania.

It is well-known that chrysoprase contains nickel ions; the nickel is what produces the color of the chrysoprases. However, ICP-AES results show that a remarkable abundance of iron and chromium may play an important role in the production of the dark green coloration of Biga chrysoprase.

In addition, the remarkable inclusion elements found in Biga chrysoprase created many peaks on its luminescence spectra due to their point defect structures. It is a highly significant finding that all major and minor photoluminescence (PL) bands decrease gradually towards a temperature of 290 K, and all photoluminescence bands undulate at a temperature of about 300 K. It was revealed that the intensity and magnitude of the PL signals increase with Fe, Cr and Mn implications which have relatively large cationic radii. When the CL luminescence activators of Biga chrysoprase are considered, it is obvious that the peak-wavelengths and intensities of CL are highly dependent on the spatially varying concentrations of K, Na and Mg rather than other metal trace impurities. As a result, it can be suggested that the remarkable CL luminescence emission in the green wavelength region (at 530 nm) in Biga chrysoprase is probably due to the silicon-oxygen and aluminium-oxygen stresses in the [SiO_4] tetrahedrons including Na, K, and Ca ions. These strained structures with Si–O bonds stabilise some non-bridging oxygen or silicon vacancy hole centres or some of the Si–O bonding defects which seem to be ultimately

responsible for this kind of electron excitation. Finally, one band peaked at 315 ^{o}C can be seen on the thermoluminescence (TL) spectrum of Biga chrysoprase. This relatively higher temperature value can be attributed to the formation conditions of the contact metamorphic zone in the Biga (Çanakkale) region. Accordingly, it can be claimed that the thermolominescence glow curve of Biga chrysoprase is one of its characteristic provenance identification methods.

REFERENCES

AMCSD (2012). *American Mineralogist crystal structure database by Downs et al.* (1993) via. <http://www.minsocam.org/MSA/Crystal_Database.html and http://rruff.geo.arizona.edu/AMS/amcsd.php>.

ASTM (1963). *Index (inorganic) to the powder diffraction file; ASTM special tech.* Pub. 48-M2, Am. Soc. for Test. and Mater, Philadelphia. pp. 244.

Arem, J.E. (1987). *Color Encyclopaedia of Gemstones, 2nd ed.* NY: Van Nostrand Reinhold. Co.

Back, M. & Mandarino, J. (2008). *Fleischer's Glossary of Mineral Species, 10th ed.* Tucson: The Mineralogical Record, Inc.

Befi, R. (2009). Australian chrysoprase with dendritic inclusions. *Gems & Gemology, 45,* 71.

Bersani, D. & Lottici, P.P. (2010). Application of Raman spectroscopy to gemology. *Analytical and Bioanalytical Chemistry, 397,* 2631–2646.

Bingol, E., Akyurek, B. & Korkmazer, B. (1973). Biga yarımadasının jeolojisi ve Karakaya Formasyonunun bazı ozellikleri. In: *Proceedings of the 50th Anniversary of the Turkish Republic Earth Science Congress*, Mineral Research and Exploration Institute of Turkey (MTA) Publications, pp. 70–77 (in Turkish).

Cady, S.L., Wenk, H.R. & Sintubin, M. (1998). Microfibrous quartz varieties: characterization by quantitative X-ray texture analysis and transmission electron microscopy. *Contributions to Mineralogy and Petrology, 130,* 320–335.

Caillaud, J., Proust, D., Philippe, S., Fontaine, C. & Fialin, M. (2009). Trace metals distribution from a serpentinite weathering at the scales of the weathering profile

and its related weathering microsystems and clay minerals. *Geoderma, 149,* 199–208.

Carter, E.A., Pasek, M.A., Smith, T., Kee, T.P., Hines, P. & Edwards, H.G.M. (2010). Rapid Raman mapping of a fulgurite. *Analytical and Bioanalytical Chemistry, 397,* 2647–2658.

Colomban, P. & Prinsloo, L. (2009). Optical spectroscopy of silicates and glasses. In: Yatwood, J., Douthwaite, R., Duckett, S. (Eds.), Spectroscopic Properties of Inorganic and Organometallic Chemistry, vol. 40. RSC Publishing, pp. 128–149.

Dean, J.A. 1999. *Lange's Handbook of Chemistry, 15th ed.* Mc-Graw-Hill, Inc. New York, pp. 743-772.

Deckert, V., George, M.W. & Umapathy, S. (2008). Raman spectroscopy at the beginning of the twenty-first century II. *Journal of Raman Spectroscopy, 39,* 1508–1511.

Heflik, W., Kwiecińska, B. & Natkaniec-Nowak, L. (1989). Color of chrysoprase. *Australian Gemology, 17(2),* 43–46 and 58–59.

Fan, J.L., Guo, S.G. & Liu, X.L. (2009). The Application of confocal micro-Raman spectrometer to nondestructive identification of filled gemstones. *Spectroscopy Letters, 42,* 129–135.

Farmer, V.D. (1974). *Infrared spectra of minerals.* Mineralogical Society, London.

Földvari, M. (1991). *Measurement of different water species in minerals by means of thermal derivatography, in Thermal Analysis in Geosciences. W. Smykatz-Kloss and S.S.J. Warne, eds.* Springer-Verlag Berlin.

Frondel, C. (1978). Characters of quartz fibers. *American Mineralogist, 63,* 17–27.

Frondel, C. (1982). Structural hydroxyl in chalcedony (Type B quartz). *American Mineralogist, 67,* 1248-1257.

Graetsch, H.A. (2011). Microstructure and origin of colour of chrysoprase from Haneti (Tanzania). *Neues Jahrbuch für Mineralogie-Abhandlungen, 188(2),* 111-117.

Gouadec, G. & Colomban, P. (2007). Raman Spectroscopy of nanomaterials: how spectra relate to disorder, particle size and mechanical properties. *Progress in Crystal Growth and Characterization of Materials, 53,* 1–56.

Gucsik, A., (Ed.). (2009). Micro-Raman spectroscopy and luminescence studies in the earth and planetary sciences. In: Gucsik, A. (Ed.), *Proceedings of the International Conference Spectroscopy 2009*, Mainz, Germany, 2–4 April, 2009, pp. 1163 (p.250).

Heflik, W., Kwiecińska, B., Natkaniec-Nowak, L. (1989). Color of chrysoprase. *Australian Gemmologist, 17(2),* 43–46 and 58–59.

Jones, J.B. & Segnit, E.R. (1971). The nature of opal I. Nomenclature and constituent phases. *Australian Journal of Earth Sciences, 18,* 57–68.

Kingma, K.J & Hemley, R.J. (1994). Raman spectroscopic study of microcrystalline silica. *American Mineralogist, 79,* 269-273.

Koçyiğit, A., Bozkurt, E. & Deveci, S. (2006). The Transition zone between the Extensional and Strike-slip neotectonic regimes in southern Marmara region: Bursa Graben. In: *International Workshop on Comparative studies of the NAF (NW Turkey) and the SAF, Southern Californi, vol. 1*, pp. 18–19.

Komov, I.L., Lukashev, A.N. & Koplus, A.V. (1994). *Geochemical methods of prospecting for non-metalic minerals.* VSP BV: The Netherlands.

Lewis, I.R. & Edwards, H.G.M. (2001). *Handbook of raman spectroscopy, from the research laboratory to the process line*. NY: Practical Spectroscopy Series. Marcel Dekker Inc.

Miehe, G., Graetsch, H. & Florke, O.W. (1984). Crystal structure and growth fabric of length-fast chalcedony. *Physics and Chemistry of Minerals, 10,* 197–199.

Lucas, A. (1989). *Ancient Egyptian materials and industries (rev. Harris J).* London: Histories and Mysteries of Man Ltd.

McMillan, P.F., & Hess, A.C. (1990). Ab initio valence force field calculations for quartz. *Physics and Chemistry of Minerals, l7,* 97-107.

Mao, H.K., Hemley, R.J. & Chao, E.C.T. (1987). The application of micro-Raman spectroscopy to analysis and identification of minerals in thin section. *Scanning Microscopy, 1,* 495-501.

Miehe, G. & Graetsch, H. (1992). Crystal structure of moganite: a new structure type for silica. *European Journal of Mineralogy, 4,* 693–706.

Mitchell, R.S. (1979). *Mineral Names What do They Mean*. NY: N.A.G. Press Ltd.

Moxon, T. & Rison, S. (1994). Moganite and water content as a function of age in agate: an XRD and thermogravimetric study. *European Journal of Mineralogy 16,* 269-278.

MSHA. (1994). Infrared determination of quartz in respirable coal mine dust: *Method P-7. Pittsburgh, PA: U.S. Department of Labour*, Mine Safety and Health Administration.

Murashov, V.V. & Svishchev, I.M. (1998). Quartz family of silica polymorphs: comparative simulation study of quartz, moganite, and orthorhombic silica, and

their phase transformations. *Physical Review B: Condensed Matter, 57,* 5639–5646.

Nagase, T., Akizuki, M., Onoda, M. & Sato, M. (1997). Chrysoprase from Warrawanda, Western Australia. *Neues Jahrbuch fur Mineralogie-Monatshaft, 7,* 289–300.

Nutall, R.H.D. & Weil, J.A. (1980). Two hydrogenic trapped-hole species in quartz. *Solid State Communications, 33,* 99–102.

Okay, A.I., Siyako, M. & Burkan, B.A. (1991). Geology and tectonic evolution of the Biga Peninsula, northwest Turkey. *Bulletin of the Technical University of Istanbul, 44,* 191–256.

Okay, A.I. & Satır, M. (2000). Upper cretaceous eclogite-facies metamorphic rocks from the Biga Peninsula Northwest, Turkey. *Turkish Journal of Earth Sciences, 9,* 47–56.

Pliny (1989). *Natural History. Jones W (translator)*. Cambridge: Harvard University Press.

Quick, L. (1974). *The Book of Agates*. Radnor-Pennsylvania: 3rd Ed., Chilton Book Co.

Sachanbinski, M., Janeczek, J., Platonov, A. & Rietmeijer, F.J.M. (2001). The origin of colour of chrysoprase from Szklary (Poland) and Sarykul Boldy (Kazakhstan). *Neues Jahrbuch fur Mineralogie Abhandlungen, 177,* 61–76.

Rapp, G. (2009). *Archaeomineralogy*. 2nd Ed., (Editors; Herrmann, B., Wagner, G. A.) Berlin: Springer-Verlag Berlin Heidelberg.

Rossman, G.R. (1994). Colored varieties of the silica minerals. Silica: Physical Behavior. *Geochemistry and Materials Applications, 29,* 433–467.

RRUFF, 2012. Database of Raman spectroscopy, X-ray diffraction and chemistry of minerals via. http://rruff.info/chrysoprase/names/asc/

Schumann, W. (1984). *Gemstone of the World*. NY: Sterling Publishing Co., N.A.G. Press Ltd.

Shigley, J.E., Laurs, B.M. & Renfro, N.D. (2009). Chrysoprase and prase opal from Haneti, central Tanzania. *Gems & Gemology, 45,* 271–279.

Skrzypek, G., Sachanbinski, M. & Jedrysek, M.O. (2003). Oxygen isotope evidence for low temperature formation of chrysoprase. *Polskie Towarzystwo Mineralogiczne–Prace Specjalne Mineralogical Society of Poland–Special Papers*, Zeszyt 22, 2003, pp. 204–206.

Skrzypek, G., Jedrysek, M.O. & Sachanbinski, M. (2004). Oxygen stable isotope geochemistry of chrysoprase from wiry and Szklary Mines (SE Poland). In: *Conference papers of International Symposium on Isotope* Hydrology and *Integrated Water Resources Management*, 19–23 May 2003, Vienne, Austria, pp.470–472.

Slodczyk, A. & Colomban, P. (2010). Probing the nanodomain origin and phase transition mechanisms in (un) poled PMN-PT single crystals and textured ceramics. *Materials, 3,* 5007–5029.

Smith, D.K. (1997). Evaluation of the detectability and quantification of respirable crystalline silica by X-ray powder diffraction. *Powder Diffraction, 12,* 200–227.

Stockton, C.M. & Fritsch, E. (1987). Infrared spectroscopy in gem identification. *Gems and Gemology, 23,* 18-26.

Taylor, D.G., Nenadic, C.M. & Crable, J.V. (1970). Infrared spectra for mineral identification. *American Industrial Hygiene Association Journal, 31,* 100-108.

Wang, A., Han, J., Guo, L., Yu, J. & Zeng, P. (1994). Database of standard Raman spectra of minerals and related inorganic crystals. *Applied Spectroscopy, 48,* 959–968.

WEBMINERAL .(No Date), (2012). Minerals arranged by X-ray powder diffraction http://webmineral.com/MySQL/xray.php.

Weil, J.A. (1984). A review of electron spin spectroscopy and its application to the study of paramagnetic defects in crystalline quartz. *Physics and Chemistry of Minerals, 10,* 149–165.

Witkowski, S. & Zabinski, W. (2004). Application of the TPR method for the studies of Ni(II) in chrysoprase. *Journal of Thermal Analysis and Calorimetry, 77,* 143–149.

Vandenabeele, P. (2010). Raman spectroscopy. *Analytical and Bioanalytical Chemistry, 397,* 2629–2630.

Yamagishi, H., Nakashima, S. & Ito, Y. (1997). High temperature infrared spectra of hydrous microcrystalline quartz. *Physics and Chemistry of Minerals, 24,* 66-74.